SANDIA REPORT

SAND2005-0337
Unlimited Release
Printed January 2005

Characterization of Soot Properties in Two-Meter JP-8 Pool Fires

Kirk A. Jensen, Jill M. Suo-Anttila, and Linda G. Blevins

Prepared by
Sandia National Laboratories
Albuquerque, New Mexico 87185 and Livermore, California 94550

Sandia is a multiprogram laboratory operated by Sandia Corporation,
a Lockheed Martin Company, for the United States Department of Energy's
National Nuclear Security Administration under Contract DE-AC04-94AL85000.

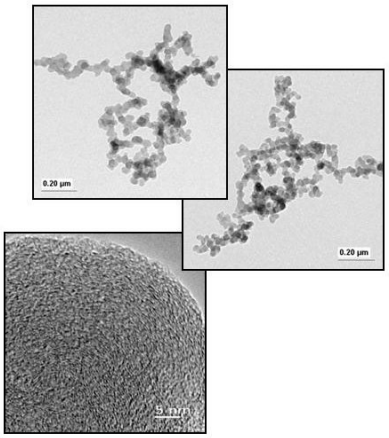

Sandia National Laboratories

Issued by Sandia National Laboratories, operated for the United States Department of Energy by Sandia Corporation.

Available to DOE and DOE contractors from
U.S. Department of Energy
Office of Scientific and Technical Information
P.O. Box 62
Oak Ridge, TN 37831

Telephone: (865)576-8401
Facsimile: (865)576-5728
E-Mail: reports@adonis.osti.gov
Online ordering: http://www.osti.gov/bridge

Available to the public from
U.S. Department of Commerce
National Technical Information Service
5285 Port Royal Rd
Springfield, VA 22161

Telephone: (800)553-6847
Facsimile: (703)605-6900
E-Mail: orders@ntis.fedworld.gov
Online order: http://www.ntis.gov/help/ordermethods.asp?loc=7-4-0#online

SAND2005-0337
Unlimited Release
Printed February 2005

Characterization of Soot Properties in Two-Meter JP-8 Pool Fires

Kirk A. Jensen and Jill M. Suo-Anttila
Fire Science and Technology
Sandia National Laboratories
P.O. Box 5800
Albuquerque, New Mexico 87185-1135

Linda G. Blevins
Combustion Research Facility
Sandia National Laboratories
P.O. Box 969
Livermore, CA 94551-9052

Abstract

The thermal hazard posed by large hydrocarbon fires is dominated by the radiative emission from high temperature soot. Since the optical properties of soot, especially in the infrared region of the electromagnetic spectrum, as well as its morphological properties, are not well known, efforts are underway to characterize these properties. Measurements of these soot properties in large fires are important for heat transfer calculations, for interpretation of laser-based diagnostics, and for developing soot property models for fire field models. This research uses extractive measurement diagnostics to characterize soot optical properties, morphology, and composition in 2 m pool fires. For measurement of the extinction coefficient, soot extracted from the flame zone is transported to a transmission cell where measurements are made using both visible and infrared lasers. Soot morphological properties are obtained by analysis via transmission electron microscopy of soot samples obtained thermophoretically within the flame zone, in the overfire region, and in the transmission cell. Soot composition, including carbon-to-hydrogen ratio and polycyclic aromatic hydrocarbon concentration, is obtained by analysis of soot collected on filters. Average dimensionless extinction coefficients of 8.4±1.2 at 635 nm and 8.7±1.1 at 1310 nm agree well with recent measurements in the overfire region of JP-8 and other fuels in lab-scale burners and fires. Average soot primary particle diameters, radiaus of gyration, and fractal dimensions agree with these recent studies. Rayleigh-Debye-Gans theory of scattering applied to the measured fractal parameters shows qualitative agreement with the trends in measured dimensionless extinction coefficients. Results of the density and chemistry are detailed in the report.

Acknowledgements

This work was supported by the Sandia Engineering Sciences Research Foundation and was performed at Sandia National Laboratories, a multi-program laboratory operated by Sandia Corporation, a Lockheed-Martin Company, for the United States Department of Energy under Contract DE-AC04-94AL85000.

The authors would like to acknowledge the contributions of the following individuals at SNL: Pat Drozda for design and fabrication of the TCRN; Tom Headley for TEM imaging of the soot samples; Andrea Irrera for quantitative analysis of the soot morphology preservation; Bennie Belone for fabrication of the screened enclosure; and David Ho for setting up the Santoro burner. Technical discussions with Chris Shaddix, Sheldon Tieszen, and John Hewson are also gratefully acknowledged. The authors would also like to recognize the contributions of the Burnsite team, consisting of Dann Jernigan, Armando Saenz, Dan Hester, and Adrian Baca. In addition, Denise Bencoe, James Hochrein, and Christine White are gratefully acknowledged for their contributions to the chemistry analysis.

Special thanks are extended to Mun Choi of Drexel University for helpful technical discussion, aiding the design of the TCRN diagnostic, and lending the Santoro burner.

Special thanks are also extended to Randy Vanderwal, Aaron Tomasek, and David Hull of the National Center for Microgravity Research at NASA Glenn Research Center for the high-resolution TEM imaging and discussion.

Our gratitude goes out to George Mulholland of NIST for his help with the calibration.

Contents

Figures

Tables

Nomenclature

D_f	Fractal dimension
d_p	Primary particle diameter (nm)
FLAME	Fire Laboratory for Accreditation of Models and Experiments
f_v	Volume fraction (m^3/m^3)
FY	Fiscal year
GC	Gas chromatograph
HAB	Height above burner
HACA	H-abstraction-C_2H_2-addition
I	Intensity of attenuated laser signal
I_o	Intensity of incident laser signal
IR	Infrared
k	Imaginary component of the index of refraction
K_e	Dimensionless extinction coefficient of soot
k_f	Fractal prefactor
L	Path length (m)
LCBS	Lurance Canyon Burn Site
m	Complex index of refraction of soot, $m = n - i\,k$
m_s , m_{soot}	Mass of soot (g)
MS	Mass spectrometry
n	Real component of the complex index of refraction
NIST	National Institute of Standards and Technology
PAH	Polycyclic aromatic hydrocarbon
PIRT	Phenomenon Identification Ranking Table
RDG-PFA	Rayleigh-Debye-Gans theory of scattering for polydisperse fractal aggregates
R_g	Radius of gyration (nm)
SIM	Selective ion monitoring
SLPM	Standard liters per minute
SNL	Sandia National Laboratories
TCRN	Transmission cell reciprocal nephelometer
TDL	Tunable diode laser
TEM	Transmission electron microscopy
V_g , V_{gas}	Volume of gas (m^3)

Greek Symbols

λ	Wavelength (nm)
ρ , ρ_s	Density of soot (g/cm^3)

I. Introduction

The thermal hazard posed by large hydrocarbon fires is dominated by the radiative emission from high temperature soot. Since the optical properties of soot are not well known, especially at infrared wavelengths where thermal radiation is important, the research described in this report focused on characterizing these properties. In addition, measurements of soot morphology and composition were completed to provide insight into soot formation processes and an assessment of the validity of the Rayleigh approximation that is commonly made in fire models. This research used extractive measurement techniques. The fires being studied were realistic in size for transportation accidents, fully turbulent, and considerably larger than previously studied. To measure the dimensionless extinction coefficient, soot was extracted from the flame zone and transported to a transmission cell, where measurements were made using both visible and near-infrared lasers. Soot morphological properties were obtained by a transmission electron microscopy analysis of soot samples obtained thermophoretically within the flame zone, in the overfire region, and in the transmission cell. Soot composition (including carbon to hydrogen ratio, polycyclic aromatic hydrocarbon concentrations, and density) was determined via analyis of soot collected on filters. Results of these measurements can be used for performing heat transfer calculations, interpreting laser diagnostic signals, and developing improved soot property models for field models of fires.

To date, measurements of the soot extinction properties have typically occurred in the overfire region of small flames, both laminar and turbulent (Mulholland and Choi, 1998; Krishnan, Lin, and Faeth, 2001). Limited measurements of the specific extinction coefficient were obtained in a larger fire (0.6 m diameter crude oil), but only in the overfire region (Dobbins, Mulholland, and Bryner, 1994). The objective of the research documented herein was to obtain measurements within the flame zone of large pool fires, thus producing a unique data set. The research provided an assessment of the variation of the soot extinction coefficient within the fire. In addition, insight into soot properties was obtained by analyzing soot morphology and composition, including carbon-to-hydrogen (C/H) ratio and targeted polycyclic aromatic hydrocarbon (PAH) concentrations.

These measurements contribute to our knowledge of heat transfer processes in fires as shown in the Phenomenon Identification Ranking Table (a.k.a., PIRT chart) listed in the FUEGO verification and validation plan (Tieszen et al., 2001). The understanding of soot formation and oxidation chemistry is ranked as high importance to abnormal thermal environments in the PIRT, and is furthered by soot morphology and composition studies with focus on soot formation, growth, and oxidation processes. Only one data set exists for soot morphology within the flame zone of a turbulent pool fire (Williams and Gritzo, 1998). Soot optical properties are also listed in the PIRT chart as having high importance, and dimensionless extinction coefficient measurements made as part of this study address this need.

II. Experimental Facility Description

The experiments were performed at the Sandia National Laboratories (SNL) Lurance Canyon Burn Site (LCBS) in the Fire Laboratory for Accreditation of Models and Experiments (FLAME) facility shown in Figure 1. The interior dimensions of the facility are approximately 6 m x 6 m x 10 m. The soot experiments were performed using a 2 m diameter pan of liquid JP-8 fuel. A controlled air source situated beneath the facility supplied inlet air at a known rate of flow and turbulence intensity (Blanchat, 2001). The fuel pan was located approximately 2.5 m from the floor, allowing the low-axial-velocity air to be entrained radially at the base of the fire. Fielding of the device in this environment was significantly more difficult than in the laboratory due to the size and duration of the fire. Because the thermal environment produced by the fires prohibited researchers from remaining in the facility, all diagnostics were remotely operated.

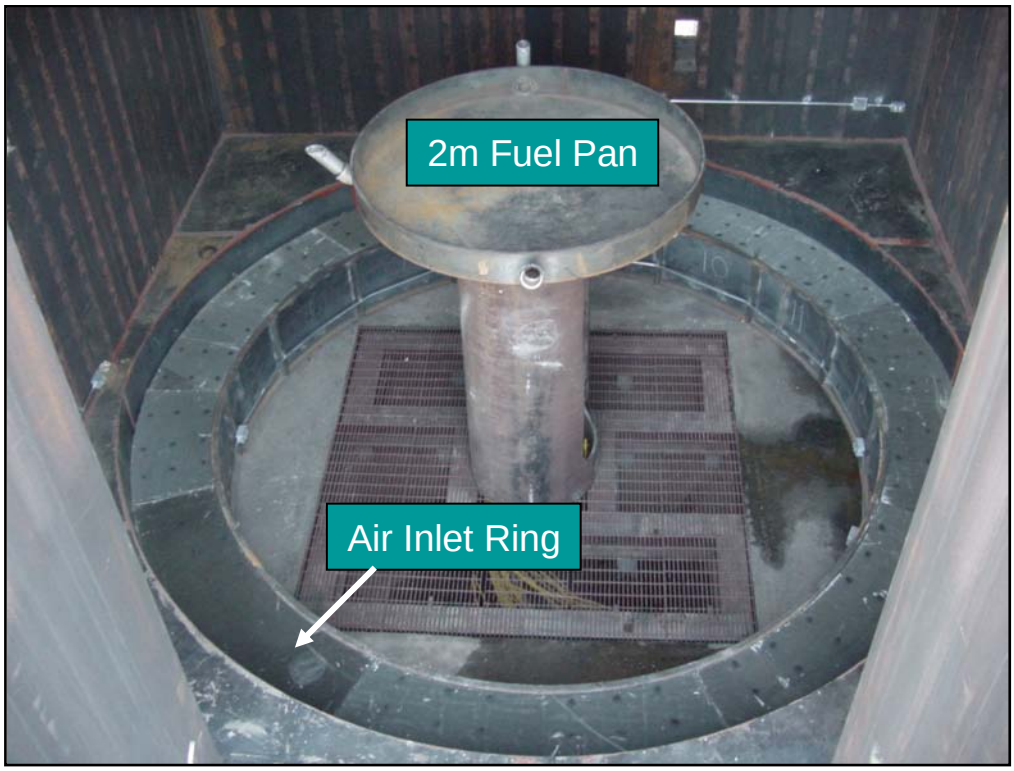

Figure 1. FLAME two-meter fire facility.

A photograph of a puff of the 2 m JP-8 fire is shown in Figure 2. Measurements were made at locations indicated by the circles at heights of 1 m, 2 m, 3 m, and in the chimney (i.e., overfire) between 5 m and 6 m above the fuel pan.

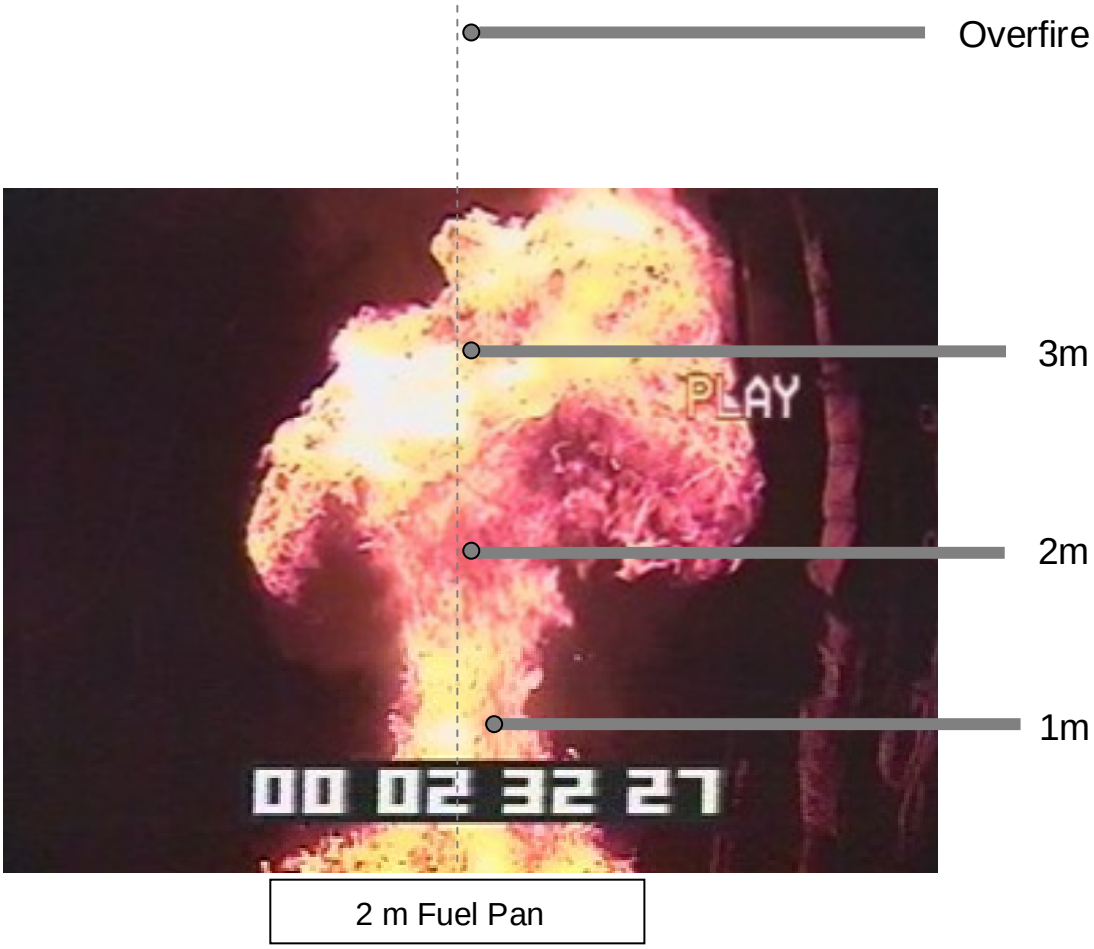

Figure 2. Two-meter fire in the FLAME facility with indication of radial location and heights above the fuel pan where measurements were performed.

III. Soot Optical Measurements

Since accurate knowledge of optical properties like the dimensionless extinction coefficient (K_e) is critical to interpreting laser diagnostic measurements (e.g., soot volume fraction, soot temperature, etc.), K_e was measured within the flame zone of 2 m diameter pool fires.

Soot particle concentrations can be measured using a non-intrusive light extinction technique where the ratio of the transmitted (I) to the incident (I_o) light intensity is used to obtain soot volume fraction (f_v),

$$\frac{I}{I_o} = \exp\left(-\frac{f_v K_e L}{\lambda}\right). \qquad (1)$$

In this equation, known as Bouguer's law, K_e is the dimensionless soot extinction constant, L is the path length through the soot, and λ is the wavelength of the light source. The accuracy of the reported soot volume fraction is highly dependent on the value used for the dimensionless soot extinction coefficient. Typically it is assumed that scattering is negligible and the extinction coefficient (equal to the absorption coefficient) can be calculated using only the complex index of refraction of soot with the following relation (Modest, 1993),

$$K_e = \frac{36\pi nk}{\left(n^2 - k^2 + 2\right)^2 + 4n^2k^2}, \tag{2}$$

where n and k are the real and imaginary components, respectively, of the index of refraction of soot, $m = n - ik$.

Based upon recent experiments at visible and near-infrared wavelengths, there are concerns about using this approach (Mulholland and Choi, 1998). The published data indicate that the measured K_e values range from 7 to 10, which is significantly larger than the value of 4.9 calculated using the previous approximate relation with a commonly accepted index of refraction $m = 1.57 - i0.56$ (Smyth and Shaddix, 1996). Additionally, there is considerable debate on the correct index of refraction for soot and whether it is dependent on fuel type, adding to the need for measurements of optical properties in large JP-8 fires.

A custom sampling system and transmission cell was used to measure the dimensionless soot extinction coefficient (K_e) in the flame zone and the overfire regions. The Transmission Cell Reciprocal Nephelometer (TCRN), was based on the specifications of Mulholland and Choi (1998). A vacuum pump extracted soot-containing gases from the fire into an uncooled sampling tube. The soot stream was diluted with N_2 gas (approximately 8:1 dilution ratio) shortly after entering the sampling tube. The diluter assembly allowed N_2 to flow evenly into the soot stream from all sides. The diluter functioned to cool the soot stream, in addition to decreasing the overall concentration, thus reducing the amount of soot deposited on the walls of the transport tube. The diluted soot stream then proceeded for approximately 10 m through the 1.27 cm diameter transport tube before reaching the diagnostic. A schematic of the soot optical diagnostic (TCRN) is shown in Figure 3.

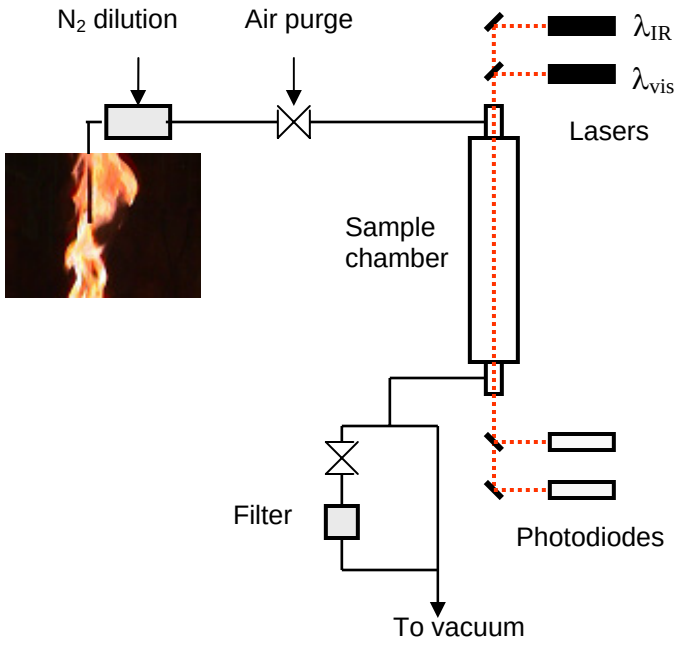

Figure 3. Soot optical properties diagnostic schematic.

The TCRN consisted of a sending optics side and receiving optics side, separated by a transmission cell through which the soot stream passed (a photograph is shown in Figure 4). The diagnostic was fabricated to be entirely modular, allowing the transmission cell length to be changed and the optics to be altered. A 1 m long transmission cell was used for the present work. The optics consisted of two diode lasers (a visible and a near-IR) and a series of mirrors and beam splitters to make the two lasers coincident before passing through the transmission cell. LaserMax laser diode light sources of 635 nm and 1310 nm were used for the extinction measurements. A Thorlabs PDA55 silicon photodetector was used to measure the transmitted visible light, while a Thorlabs PDA400 InGaAs detector was used to measure the IR laser light. The soot stream exiting the transmission cell was deposited on a glass fiber filter contained in a Gelman Sciences 47 mm stainless steel housing. The flow through the filter was adjusted by a mass flow controller with a range of 0-5 L/min. The filter flow controller was linked to the flow controller supplying N_2 to the diluter to permit a constant flow and dilution. The volume fraction of the soot was calculated using the rate of flow through the filter (monitored by a data acquisition system) and the mass of soot collected on the filter (measured using a Mettler model H64AR balance with a resolution of 0.01 mg). Typical sample masses collected were 1-2 mg. The K_e value was calculated from Equation 1 using the attenuation, path length, wavelength, and the gravimetrically determined soot volume fraction.

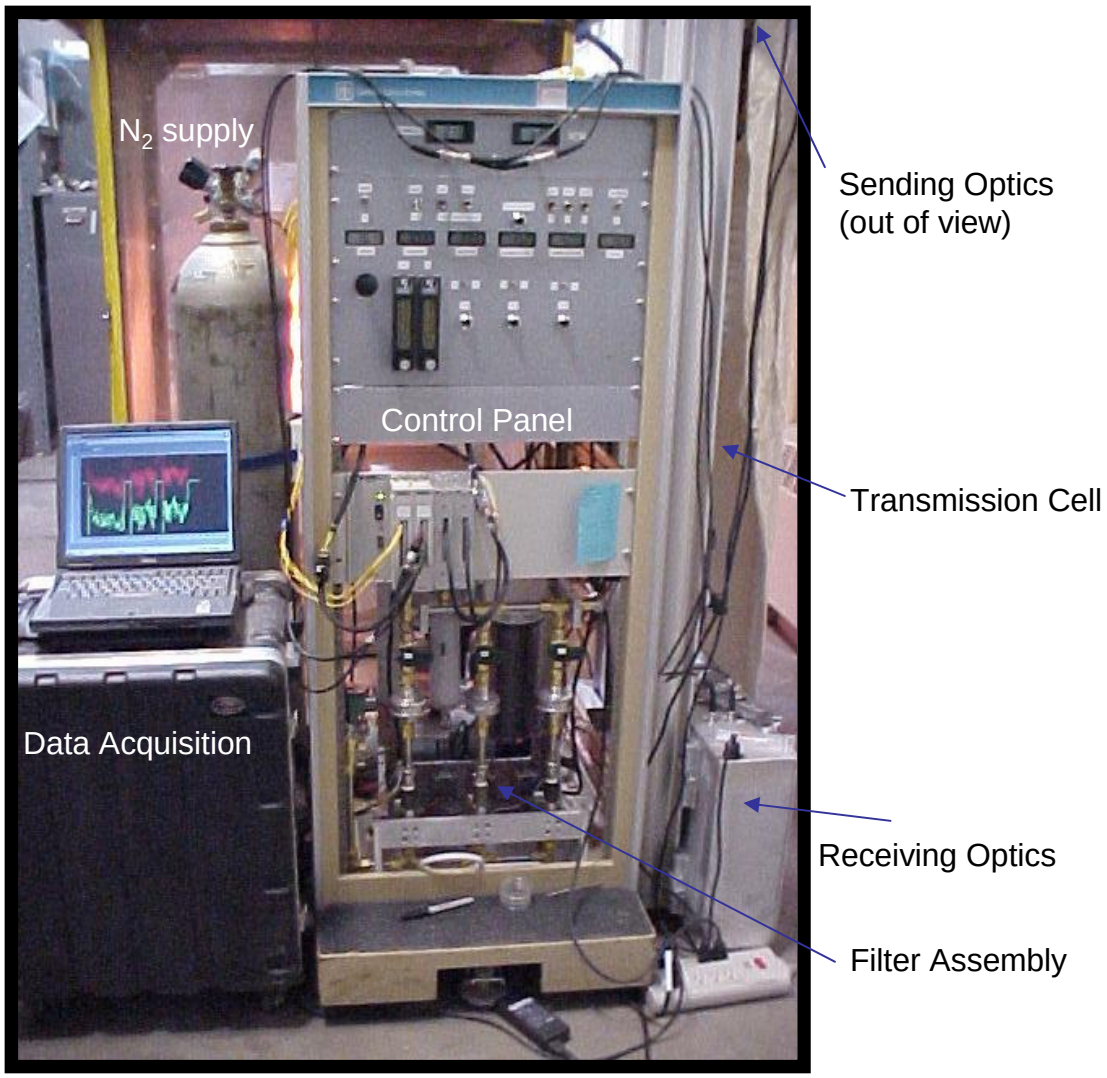

Figure 4. Photograph of soot optical diagnostic for measuring the dimensionless extinction coefficient.

The design permitted either nitrogen purge or a soot-containing gas sample from within the fire to pass through the transmission cell at any given time. All solenoid valves, controlling flow through the box and deposition on the filters, were remotely activated from the control panel.

IV. Soot Morphology Measurements

Knowledge of soot morphology allows for interpretation of the growth mechanism of the agglomerates and an assessment of the Rayleigh limit approximation typically used in fire model radiation heat transfer calculations. Studies of soot morphology have previously been performed within the flame zone of small laminar or turbulent flames or within the overfire region of larger fires (Köylü and Faeth, 1993; Faeth and Köylü, 1995). Analysis of soot morphology within the flame zone of fully turbulent fires (> 1 m diameter) is quite limited (Williams and Gritzo, 1998) and does not include an assessment of the variation of soot morphology with position in the flame. Such data would provide additional insight into soot formation, growth, and agglomeration processes.

To meet this need, soot was thermophoretically sampled within the flame zone of the fires to assess the morphology, including the extent and character of soot agglomeration. The thermophoretic sampler used in this study is based on the design of Dobbins and Megaridis (1987) with minor modifications to simplify holding the grid in larger flames. Figure 5 shows a schematic of the sampler and a photograph of the grid holder section attached to the air cylinder. The grid is exposed to the fire for a short duration (on the order of 1/10 s) such that soot is deposited thermophoretically. The grid is subsequently imaged using a Transmission Electron Microscope (TEM) for analysis. Thermophoretic sampling in large pool fires was first demonstrated by Williams and Gritzo (1998).

In the present work, a solenoid-actuated piston-cylinder assembly with pressurized N_2 gas activation was used to quickly expose the electron microscope grid to the flames of a fully turbulent large pool fire. The two copper TEM grids (approximately 3 mm in diameter and 0.11 mm thick) were mounted to a 0.32 cm thick grid holder using a 0.08 cm thick aluminum plate. The grids were oriented with the carbon substrate side against the upper plate for protection of the delicate film. The grid holder was fastened to a non-rotating rod of the air cylinder and was enclosed in a 25 cm long, low-flow, N_2-purged protective housing. Two baffles were positioned at the exit of the protective housing to reduce the probability of stray soot particle deposition on the grids prior to fire exposure. During sampling, the air cylinder was pressurized such that the grids were extended 8 cm from the end of the protective housing for 0.1 sec. Following the fire experiment, the grids were removed from the holder and directly inserted in the TEM for analysis.

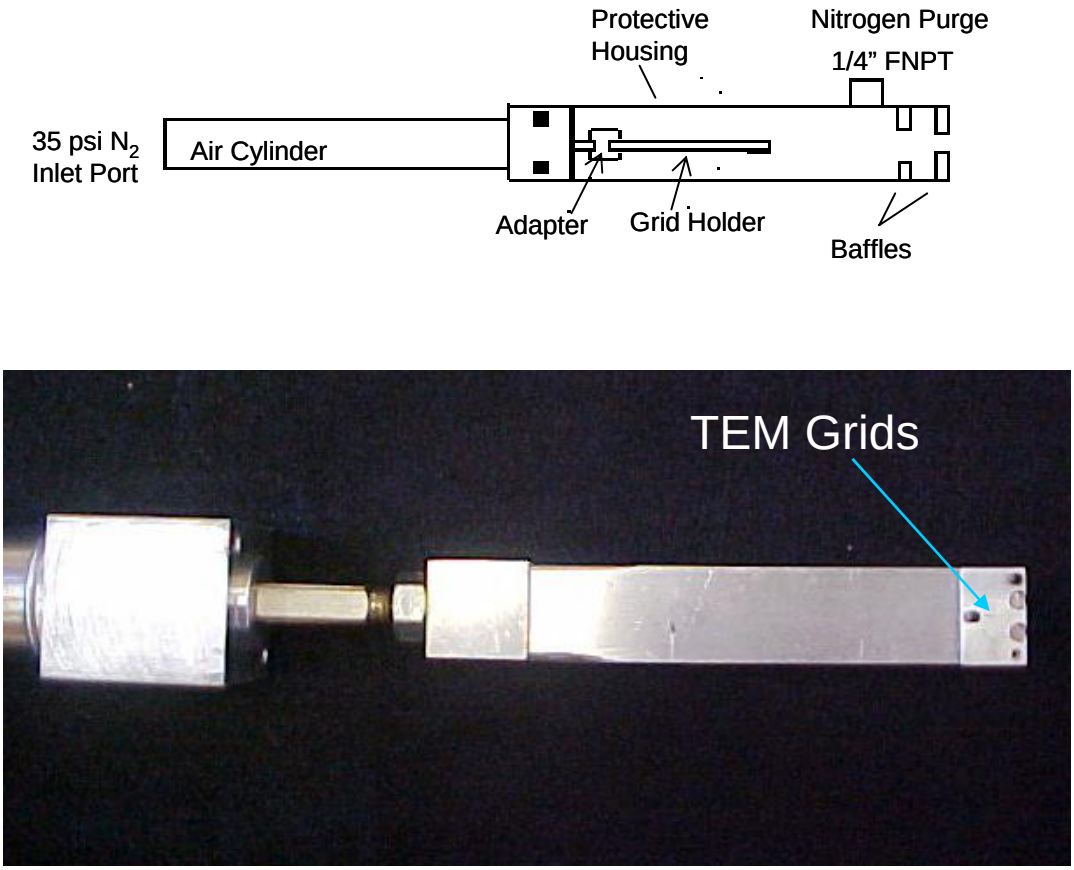

Figure 5. Schematic of the thermophoretic sampler for collecting soot from the flame zone of large fires and photograph of the grid holder attached to the cylinder.

Soot properties of interest include the dimension and projected area of primary particles and aggregates since they influence the optical properties. Figure 6 shows a typical soot aggregate obtained from the microscopy. A large quantity of similar digital images was obtained from randomly selected aggregates on the grids sampled at each location in the fire. Using custom imaging software, a screen from which is also shown in Figure 6, the soot aggregate radius of gyration (R_g) and primary particle diameter (d_p) were determined directly from each TEM image. In addition, the fractal-like properties of the soot were calculated from a large set of aggregates at each height with the same software by combining R_g and d_p from the individual TEM images.

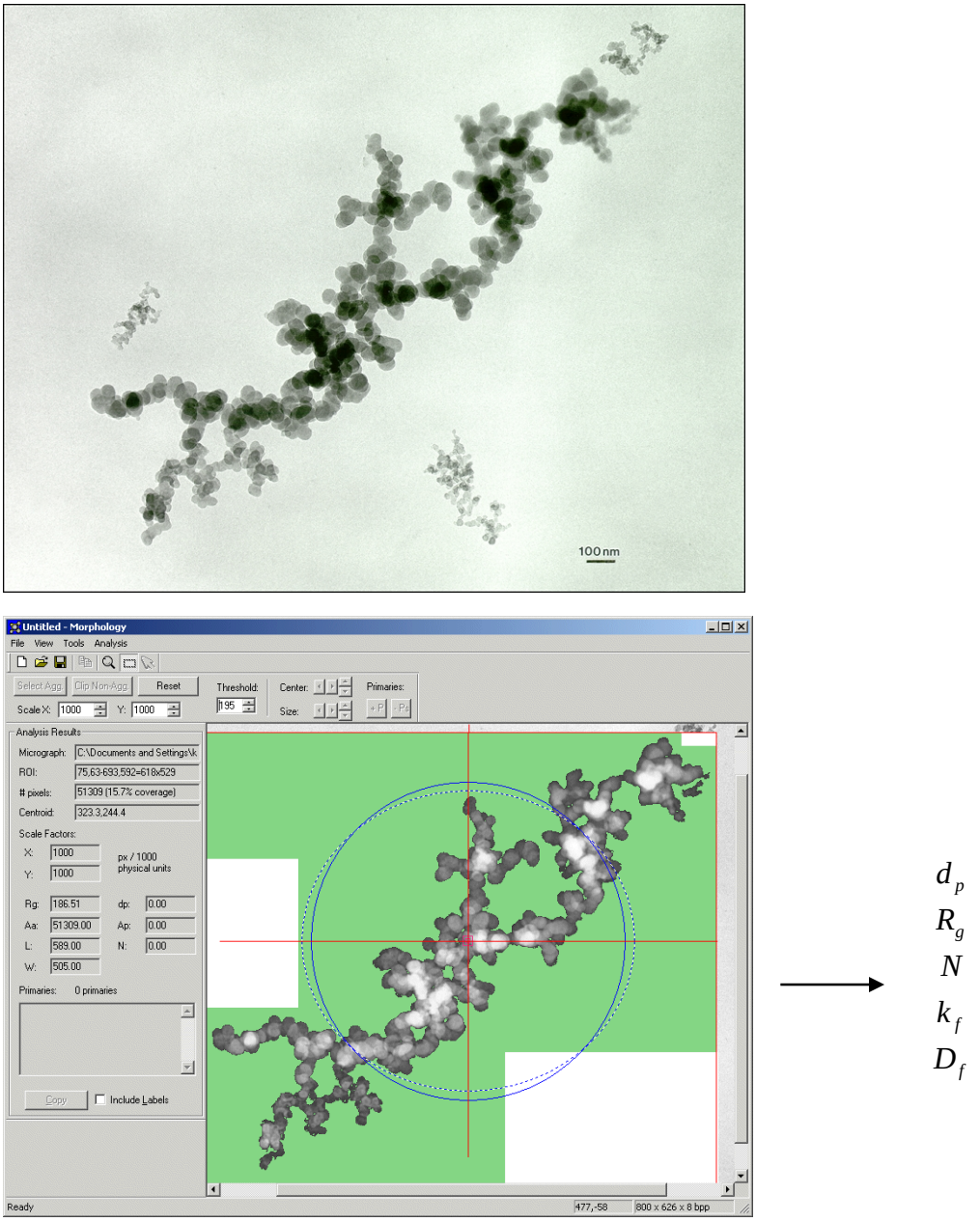

Figure 6. Soot aggregate and analysis software.

Soot aggregate structure is too sparse for it to be described as a compact sphere, thus mass fractal analysis provides a useful relationship to determine the radius of gyration (R_g) based on primary particle size and the number of primary particles comprising the aggregate,

$$R_g = \sqrt{\frac{1}{N}\sum_{i=1}^{N}(r_i - r_c)^2}\ , \tag{3}$$

where r_i is the centroid of the primary particle, r_c is the centroid of the agglomerate, and N is the total number of particles comprising the aggregate. Since it is difficult to identify each individual particle that constitutes an aggregate, the R_g calculation formulation was revised by considering each pixel to be the individual element of interest (Choi, 2002; Manzello and Choi, 2002). This approximation is valid since the average contribution to the total R_g from the sub-elements (pixels) that constitute the primary particle is equal to the contribution from a primary particle to the total R_g. The equation for the radius of gyration remains the same but N (determined by performing a histogram distribution of all pixels with graylevel less than the background threshold) now corresponds to the total number of pixel elements comprising the agglomerate (typically on the order of 20-30 thousand pixels).

Finally, the fractal prefactor (k_f) and the fractal dimension (D_f) can be determined based on the following relationship (Dobbins, et al. 1994),

$$N = k_f \left[\frac{R_g}{d_p} \right]^{D_f} \tag{4a}$$

where the number of primary particles in the aggregate, N, is determined from the emperical relationship (Manzello and Choi, 2002)

$$N = \left[\frac{A_a}{\pi d_p^2 / 4} \right]^{1.09} \tag{4b}$$

where A_a is the projected area of the aggregate (i.e., the number of pixels comprising the aggregate times its dimensions. The logarithm of both sides of Equation 4a reveals a linear relation,

$$\log(N) = D_f \cdot \log\left(\frac{R_g}{d_p} \right) + \log(k_f). \tag{5}$$

On a scatter plot of log(N) versus log(R_g /d_p) for a large number of aggregates, the fractal dimension, D_f, is the slope of the line, and the intercept has the value of log(k_f).

V. Soot Composition Measurements

Most previous studies of soot chemistry have been undertaken using small laboratory flames with gaseous or pure liquid fuels (Frenklach, M., 2002; Richter, H., and Howard, J.B., 2000; Kennedy, I.M., 1997; Glassman, I.,1988; Haynes, B.S., and Wagner, H.G., 1981; Calcote, H.F., 1981). The present study aims to examine soot chemistry in a more complex flame (buoyant, turbulent pool fire) burning with a multi-component fuel (JP-8).

As part of the measurement for the dimensionless soot extinction coefficient, soot was collected on a filter. The soot samples collected on the filters were then analyzed for carbon-to-hydrogen (C/H) ratio and polycyclic aromatic hydrocarbon (PAH) concentrations to gain insight into soot formation processes and determine the potential impact on the optical properties. Pall Corporation Zefluor filters (#P5PL047) were selected for use in the experiments. Glass fiber filters were also examined since they provided less flow restriction, but they were deemed unsuitable since they were very fragile and fibers were easily lost during handling. Bulk samples of deposited soot were collected over the duration of the fire at different locations to facilitate soot density measurements needed to calculate the dimensionless extinction coefficient calculations. Details of each individual measurement technique are described in the sections that follow.

A. Carbon to Hydrogen Analysis

The filter soot samples were analyzed for C/H ratio to gain insight into their extent of carbonization and its potential impact on the optical properties. For reference, it is noted that soot precursor particles typically have a C/H ratio of about 2.0, while carbonaceous soot generally has a molar C/H ratio greater than 5.0. Additional discussion of soot C/H ratio can be found in a recent paper (Blevins, et al., 2002). Their research determined that the C/H ratio from laminar, inverse diffusion flames (formed at the interface of an air jet surrounded by ethylene co-flowing in an annulus) was approximately 2.2, a value typical of soot precursor particles. It is possible that regions mimicking inverse and normal diffusion flames might occur in a large, turbulent pool fire.

Soot was analyzed at SNL using a Perkin Elmer 2400 Series II CHNS/O analyzer, shown in Figure 7. The analyzer was configured to run in CHN mode (i.e. no S or O analysis). Soot was prepared for analysis by scraping a sufficient amount off the filter and placing it into a small, thin aluminum dish. The dish was folded into a small square and placed in an auto carousel to be placed into the combustion tube of the analyzer. The analyzer combusts samples in an O_2 environment and then transports the combustion products through a gas chromatograph (GC) column, where the CO_2 and H_2O concentrations are measured with a thermal conductivity detector. The C and H amounts are calculated from these concentrations.

An analysis of the soot by an outside company was also performed for comparison purposes. This evaluation used a procedure involving water jet impingement followed by

heating, and was later deemed unsuitable because of possible pyrolysis during the heating step; therefore, the results from the outside company will not be presented.

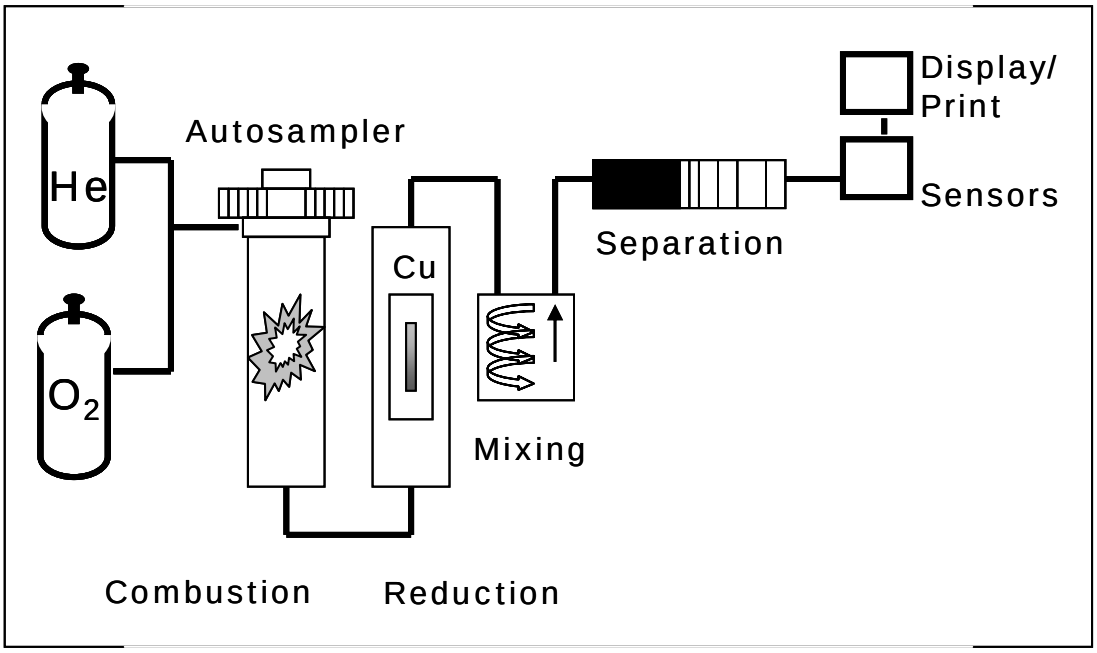

Figure 7. Schematic of CHN analyzer.

B. Polycyclic Aromatic Hydrocarbons (PAH) Concentration Analysis

Filter samples containing soot were also analyzed for PAH concentrations. The PAH were extracted from the filters using a mixture of methanol and toluene and analyzed using gas chromatography/mass spectrometry (GC/MS). The PAH concentrations at different elevations within the fire could provide insight into soot formation processes. PAHs are believed to be the building blocks of soot and can contribute to soot size growth by attachment to the outer surface of the soot particles as described in detail by Richter and Howard (2000). Further description of the PAH analysis can be found in Hochrein and Borek (2003).

Reference Sample Preparation

The reference standard used was a 2000 ppm certified Supelco PAH mix. The Supelco mix solvent, methylene chloride, was evaporated using N_2. Once the methylene chloride was removed, a 200 ppm reference solution was made with a 10:1 mass-to-mass serial dilution using the 6:1 methanol-toluene solvent system. This serial dilution method was repeated to make 20 ppm, 2 ppm, 200 ppb, 20 ppb, and 2 ppb reference solutions which were also analyzed for comparison and to determine limits of detection. A standard curve was constructed for each identified compound using serial mass-to-mass dilutions to obtain a working concentration range of about 2000 ppm-20 ppb. Peak areas were integrated and plotted against concentration to generate a standard curve. Peak areas from the samples were entered into the standard curve equation and resulting concentration

values were generated. Gravimetrically obtained soot masses were used to calculate final concentrations expressed in μg PAH per mg of soot. PAHs expected to be significant, and which can be analyzed in the GC/MS setup, referred to as "target" or "targeted" PAHs, are shown in Table 1. The molecular structure diagrams shown in the table for 1-methylnaphthalene and 2-methylnaphthalene were obtained from the NIST chemistry web book (http://webbook.nist.gov/) and the rest were obtained from Sander and Wise (1997, also http://ois.nist.gov/pah/).

Except for 1-methylnaphthalene ($C_{11}H_{10}$, 142 g/mol), 2-methylnaphthalene ($C_{11}H_{10}$, 142 g/mol), and fluorene ($C_{13}H_{10}$, 166 g/mol), the targeted PAHs consist of even numbers of carbon and hydrogen atoms, which are more stable than their odd-carbon counterparts (Stein and Fahr, 1985). Additionally, naphthalene is the most thermodynamically stable $C_{10}H_8$ isomer, acenaphthylene is the most stable $C_{12}H_8$ isomer, anthracene is the most stable $C_{14}H_{10}$ isomer, pyrene is the most stable $C_{16}H_{10}$ isomer, and chrysene is the most stable $C_{18}H_{12}$ isomer (Stein and Fahr, 1985). The most stable $C_{20}H_{12}$ isomer, benzo[e]pyrene, is not targeted in the reference standard, although its' less stable benzo[a]pyrene and benzo[b]fluoranthene $C_{20}H_{12}$ counterparts are targeted. Five of the targeted compounds (acenaphthylene, acenaphthene, fluorene, fluoranthene, and benzo[b]fluoranthene) contain five-carbon rings. Such five-membered rings may contribute to PAH molecular growth (Frenklach, 2002) or cause molecular stresses that cause molecules to curl and arrange themselves into shell-like shapes.

Once the most thermodynamically stable isomers are formed, they are not likely to disassociate at flame temperatures (Frenklach, 2002). Hence, they may be key contributors to soot inception and/or surface growth. Low in the center and in the annulus of ethylene diffusion flames, Dobbins and coworkers (1998) found liquid-like precursor particles that contained PAH distributions consistent with stabilomer components. It has been hypothesized that soot inception occurs when two- and three-ring resonantly stabilized aromatic radicals link together with aliphatic bonds in open structures. These structures grow to yield nanoparticles that eventually carbonize upon heating (D'Anna et al., 2001). This theory is consistent with Dobbins' discovery of PAH-laden precursor particles (Dobbins et al., 1998) if the assumption is made that the young nanoparticles are fragmented into their aromatic building blocks during Dobbins' laser microprobe mass spectrometry (D'Anna et al., 2001). Soot surface growth can take place through a chemical mechanism similar to the HACA PAH growth mechanism if one assumes the surface of the particle is analogous to that of a hydrocarbon molecule (Frenklach, 2002). A point of controversy in the soot literature is whether PAH concentrations are likely (Richter and Howard, 2000) or unlikely (Frenklach, 2002) to contribute to soot particle surface growth.

PAH like those in the table have recently been shown to not absorb photons with a wavelength of 1310 nm at room temperature (Lee, et al., 2003). Additionally, they are not expected to absorb 635 nm light since such PAH absorb ultraviolet light but stop absorbing significantly at wavelengths lower than 635 nm (Ciajolo, et al., 1994). Hence, the presence of PAH is not expected to affect the 1310 nm and 635 nm soot optical properties measured during the present work.

Table 1. Target polycyclic aromatic hydrocarbons (PAHs).

Compound	MW	Formula	# rings	BP, °C	Structure
Naphthalene	128	$C_{10}H_8$	2	218	
a-Methylnaphthalene	142	$C_{11}H_{10}$	2	240-243	
2-Methylnaphthalene	142	$C_{11}H_{10}$	2	241	
Acenaphthylene	152	$C_{12}H_8$	3	265	
Acenaphthene	154	$C_{12}H_{10}$	3	279	
Fluorene	166	$C_{13}H_{10}$	3	295	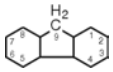
Anthracene	178	$C_{14}H_{10}$	3	340	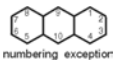
Phenanthrene	178	$C_{14}H_{10}$	3	340	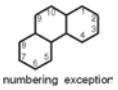
Fluoranthene	202	$C_{16}H_{10}$	4	375	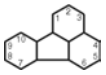
Pyrene	202	$C_{16}H_{10}$	4	404	
Benzo[a]anthracene	228	$C_{18}H_{12}$	4	437	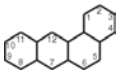
Chrysene	228	$C_{18}H_{12}$	4	448	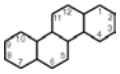
Benzo[a]pyrene	252	$C_{20}H_{12}$	5	495	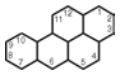
Benzo[b]fluoranthene	252	$C_{20}H_{12}$	5	357	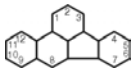

Sample Preparation

The filters were extracted using a newly developed microwave method (Hochrein and Borek, 2003). Filters were placed into extraction vessels with the 6:1 methanol toluene mixture and were sonicated for 15 minutes. Samples were then prepared with about 0.03 g of perdeuterated PAH solution. The PAH was added to the solution to determine extraction efficiency, provide an analytical reference, and verify the instrument operability. The extraction vessels were then tightly sealed and placed in the microwave for extraction. The extraction method used 1200 watts of power, ramped to 1.3 MPa (175 psig) and 180°C in five minutes, and held these conditions for 15 minutes. This operation is followed by a 15-minute cool-down period. Filters were then removed from

the vessels and the solutions were transferred to vials and centrifuged to remove soot particulates. The extraction solution was evaporated to dryness using a dry N_2 purge evaporator, and then brought back up to 0.1 ml using 6:1 methanol toluene solution. Each extract was placed in a vial and analyzed by GC/MS.

Gas Chromatography with Mass Spectrometry Detection Analysis

Due to the relatively low concentrations of PAHs in the soot samples, selective ion monitoring (SIM) was used to decrease interferences and increase sensitivity. Absolute identification may be made for an organic compound if two criteria are met: the retention time of an unknown compound matches the retention time of a known standard; and the mass spectra match. The analysis was carried out for each reference compound and sample using the method shown in Table 2.

Table 2. Selective ion monitoring (SIM) procedure.

INSTRUMENTATION: ThermoFinnigan SSQ, gas chromatograph/quadrapole mass spectrometer					
GC Column: J&W Scientific, DB-5ms column, 60m x 0.25 mm, 1 µm df					
Temperatures	Oven Init.	Oven Ramp	Oven Final	Injector	Transfer line
	80°C for 1.0 min	25°C/min to 160°C then 5°C/min to 300°C	300°C for 30.0 min	280°C	280°C
Injection Volume : 1 µL, splitless					
Carrier Gas: Helium at 29 psi constant pressure					
Filament Delay: 6.0 minutes					
Source Temperature: 150°C					
Manifold Temperature: 70°C					

Due to limitations of the GC/MS, analysis of all PAH's had to be performed in a two-step sequence using two different SIM profiles. Figure 8 shows the analysis of the PAH reference solution and six target PAH compounds (masses 128, 142, 152, 154, and 166). The bottom chromatogram is from a typical sample. The top chromatogram is the Supelco PAH mix standard reference material. The bottom chromatogram shows corresponding PAH's that were identified from the filter. All target PAH's were identified in this sample.

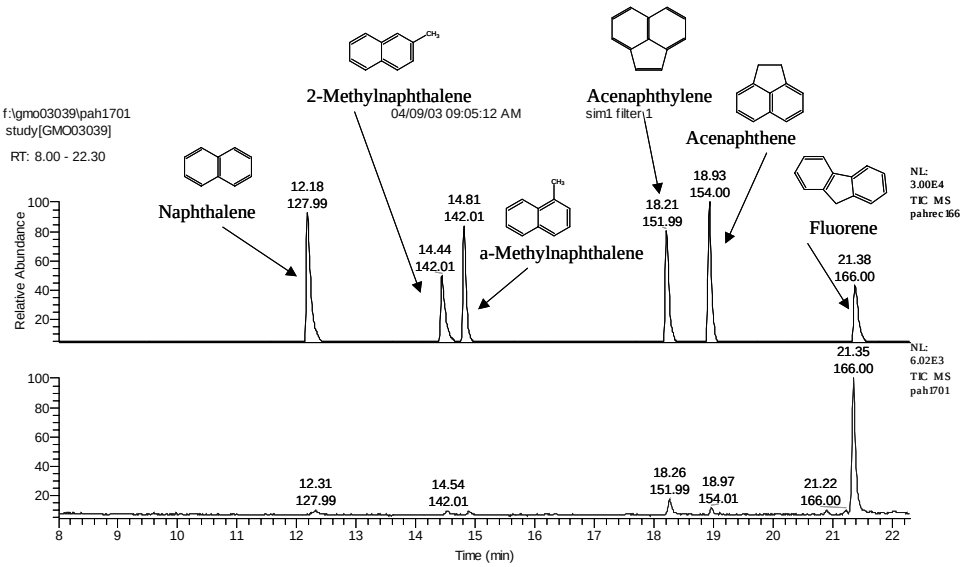

Figure 8. Chromatograms of PAH mix (top) and a filter (bottom).

Figure 9 shows the same two solutions re-analyzed with the second SIM profile for masses 178, 202, 228, 252, and 278. The top chromatogram is the Supelco PAH mix standard reference material. The bottom chromatogram shows corresponding PAH's that were identified from filter 1. All target PAH's were identified in this sample.

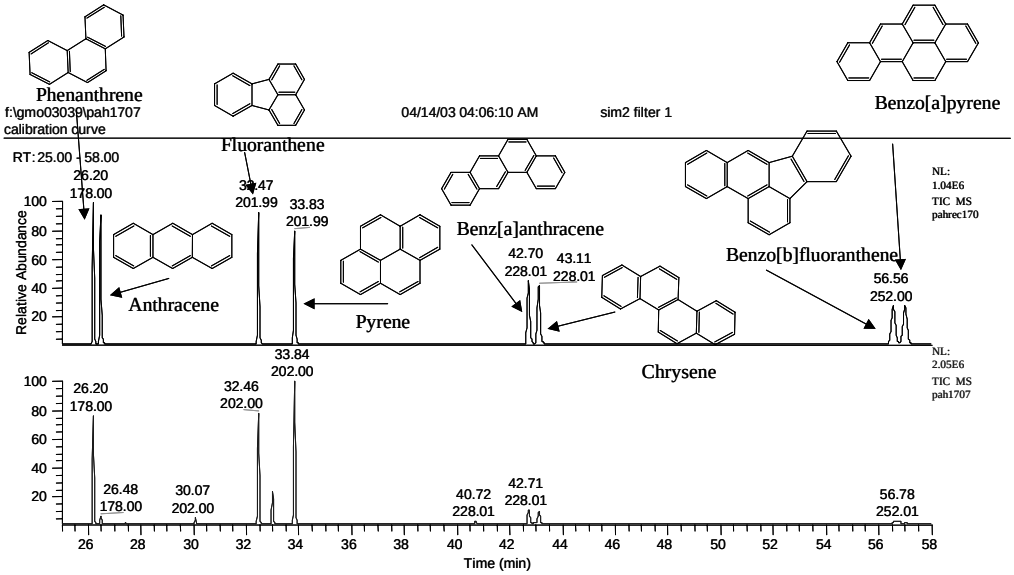

Figure 9. Chromatograms of PAH mix (top) and a filter (bottom).

C. Soot Density Analysis

Another important property of soot is the density. A density value is required in the calculation of K_e to compute the volume of soot from the measured mass of soot. The density of soot in the experiments was measured to provide confidence in the value used in the calculation of K_e. Soot density values reported in the literature commonly range

from 1.7 g/cc to 2.1 g/cc. Inadequate knowledge of the soot density could result in a large uncertainty in the calculated optical properties (K_e). Soot density determination can not simply be performed using a filter collection as was done for C/H and PAH measurements since a very large amount of soot must be collected for a density measurement. Soot was scraped from the exposed end of the sampling tube and other components near the sampling point to obtain an adequate quantity. Density analyses were performed by two individual laboratories according to the procedures outlined below.

The helium pycnometer used by SNL was a Quantachrome Ultrapycnometer 1000. The analysis was conducted as described below:

- The soot samples were placed in alumina dishes and kept in an 85-90 ºC oven to keep them dry until ready to perform the measurement.
- The warm soot was placed in the small non-elutriating sample cell (less than 10 cm^3 volume capacity).
- The sample was weighed and placed into the pycnometer with the non-elutriating cover placed over the sample.
- The sample was allowed to equilibrate to room temperature in a helium atmosphere (60 min).
- The actual data run was started. The run consisted of 50 pulses of helium to further purge the soot of air (recommended by Quantachrome for fine powders). Ten density measurements were then performed.
- After the data were recorded, a second consecutive run was conducted using the same run parameters, i.e., 50 pulses followed by ten density measurements.

A second analysis was conducted by Porous Materials Incorporated utilizing a PMI gas pycnometer model GYC G 100A and the following procedure.

- A group of filter holders containing soot were provided for each fire experiment.
- Soot from the supplied filter holders was combined and two representative samples from the test were obtained.
- The tested sample from this combination was packed by tapping on a table top.
- The sample chamber filled with the soot and the volume of the sample chamber was documented.
- Twenty iterations of each measurement were performed.
- Pressure was stabilized between each test.
- Each sample was analyzed twice without removing it from the apparatus.

VI. Experimental Uncertainty

An uncertainty analysis was performed using the method described by Coleman and Steele (1999) and Taylor and Kuyatt (1994). The magnitude of the Type A uncertainty, or random uncertainty, will be described in the results section where the standard deviations and the mean values are presented. This section concentrates on the Type B uncertainty, or systematic uncertainty. Parameters contributing to the Type B uncertainty are primarily based on manufacturer's specifications for the components within the diagnostic.

As described earlier, the soot particle concentrations can be measured using a non-intrusive light extinction technique where the ratio of the transmitted to the incident light intensity is used to obtain soot volume fraction.

The research presented here measures the dimensionless extinction coefficient via a rearrangement of the Equation 1,

$$K_e = \frac{-\lambda \rho_{soot} V_{gas} \ln \frac{I}{I_o}}{L m_{soot}}. \tag{6}$$

The uncertainty in calculating K_e using Equation 7 can be determined with knowledge of the uncertainty in each of the individual terms. Assuming that the different variables are uncorrelated, the overall uncertainty in the K_e calculation is expressed as

$$\frac{\delta K_e}{K_e} = \sqrt{\sum_n \left[\frac{S_n}{K_e} \cdot \frac{\partial K_e}{\partial S_n} \cdot \frac{\delta S_n}{S_n} \right]^2}, \tag{7}$$

where δK_e is the total uncertainty in K_e, S_n is the parameter associated with the nth source, and δS_n is the uncertainty of the parameter.

A summary of the individual terms in the above equation is shown in Table 3. The individual uncertainties were based on manufacturer specifications. Values for each variable used in the computation of the percent uncertainty for each variable (denominator in the last column) were based upon average or actual experimental values. The wavelength used was 635 nm, gas volume was 5 L/min, density of soot was 1.74 g/cm^3, path length was 1 m, mass of soot was 1 mg, the attenuation was 0.5, and laser signal was 4 volts. The total uncertainty was calculated using columns 3 and 5 in the table as shown in the equation below.

$$\frac{\delta K_e}{K_e} = \sqrt{(0.016)^2 + (0.115)^2 + (0.015)^2 + (-1 \cdot 0.013)^2 + (-1 \cdot 0.022)^2 + \left(\frac{1}{\ln 0.5} \cdot 0.00068 \right)^2} \tag{8}$$

The largest contributor to the experimental uncertainty is the density of the soot. Other possible systematic uncertainties not accounted for in the analysis include multiple scattering effects and forward scattering over the finite acceptance angle of the detector (Bohren and Huffman, 1983).

Table 3. Summary of Type B experimental uncertainties.

Source S	$\frac{\partial K_e}{\partial S}$	$\frac{S}{K_e}\cdot\frac{\partial K_e}{\partial S}$	Components of Uncertainty in S	$\frac{\delta S}{S}$
λ	$\frac{-\rho_{soot} V_{gas} \ln\frac{I}{I_o}}{L m_{soot}}$	1	Laser specs $\pm$ 10nm	0.016
ρ_{soot}	$\frac{-\lambda V_{gas} \ln\frac{I}{I_o}}{L m_{soot}}$	1	Literature and current study $\pm$ 0.2 g/cm^3	0.115
V_{gas}	$\frac{-\lambda \rho_{soot} \ln\frac{I}{I_o}}{L m_{soot}}$	1	Accuracy $\pm$1.5 % FS Resolution 0.01 L/min	0.015
L	$\frac{-\lambda \rho_{soot} V_{gas} \ln\frac{I}{I_o}}{L^2 m_{soot}}$	-1	Fabrication $\pm$ 0.125” Purge fluctuation $\pm$ 0.5”	0.013
m_{soot}	$\frac{-\lambda \rho_{soot} V_{gas} \ln\frac{I}{I_o}}{L m_{soot}^{\ 2}}$	-1	Resolution 0.01 mg Repeatability 0.02 mg	0.022
$\frac{I}{I_o}$	$\frac{-\lambda \rho_{soot} V_{gas}}{L m_{soot}}\cdot\frac{I_o}{I}$	$\frac{1}{\ln\frac{I}{I_o}}$	Detector resolution 0.0001 V Detector noise 0.00033 V	0.00068
			Total uncertainty (%)	**11.9**

The calculated total uncertainty in the K_e measurement due to Type B uncertainty is 11.9%. The accuracy of these measurements would greatly benefit from more accurate soot density measurements.

VII. Experimental Setup at the FLAME Facility and Test Matrices

Several adaptations were made to the soot optical diagnostic during the course of the present research. The diagnostic was characterized in 30 cm lab scale pool fires before operation in the larger 2 m fires at the FLAME facility. The portability of the device was improved through the design and fabrication of a fixture to house all of the diagnostic components. All of the diagnostic components are now contained within a single, portable rack. A control panel was manufactured to allow accurate adjustment of all flow meters and switches. The robustness of the device was improved by modifying the optics and transmission cell mounts. These modifications allowed the diagnostic to be transported to the Burn Site without damage or significant changes in the optics alignment. In addition, using calibrated mass flow controllers and a high-resolution scale further reduced the uncertainty in the optical property measurements.

The picture on the left side of Figure 10 shows the pole where the soot sampler tube for the TCRN and the TEM sampler are mounted in the 2 m fires in the FLAME facility. On the right side of the figure, the fuel pan and air source are shown in the lower image, and a frontal profile of the diagnostic is in the upper image. Note that the sampling tube (pointing down) for the TCRN sits outside the white Kaowool insulation to keep the extraction process at higher temperatures until the soot reaches the N_2 diluter outside the FLAME building. The flow tubing continues outside of FLAME from the diluter to the optical chamber of the TCRN in the diagnostics trailer on the west side of the facility.

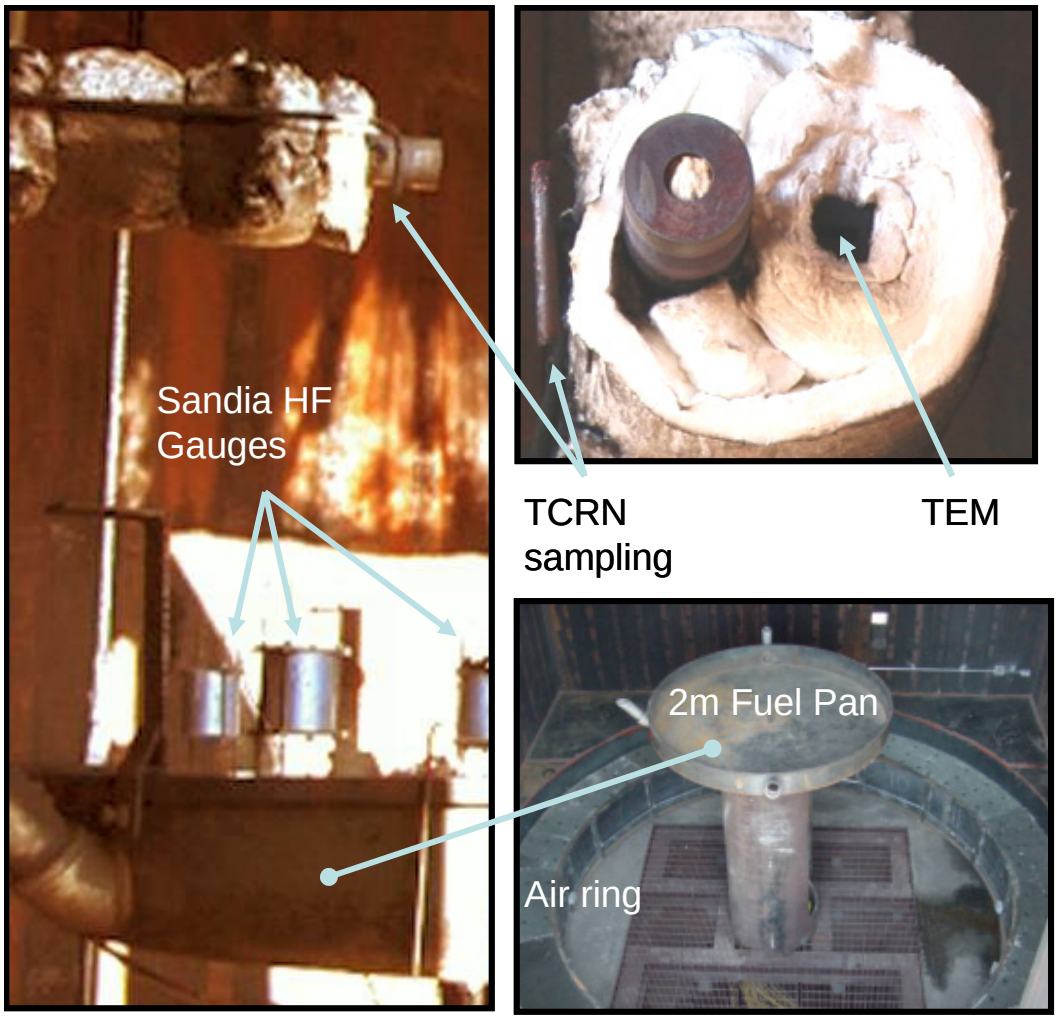

Figure 10. Soot sampling diagnostics installed in the FLAME facility.

The diagnostics were approximately 10.2 cm (4 inches) off center at the 2 m and 3 m height measurement locations (they could not reach the center because of physical limitations). In the overfire location, the measurements were performed in the center of the chimney. At the lowest height of 1 m, the diagnostics were positioned 30.5 cm (12 inches) away from the center due to difficulties collecting soot along the centerline. It is believed that at this lower height the probe was still positioned in the vapor dome of the large fire which prohibited the collection of reliable data.

A. Test Matrix for August 2002

The TCRN soot diagnostic was initially set up in FLAME in August 2002 to take advantage of a series of fires already being performed to troubleshoot installation and operation of the Tunable Diode Laser (TDL) probe in the large scale test environment. The measurement locations and fire durations were dictated by the TDL support staff. Sensitivity of the TDL optics to high temperatures limited these tests to shorter fires. During these shorter fires, it was found that one or two soot sampling measurements

could be performed for a duration of two or three minutes each during the steady portion of the fire. The measurement locations were chosen to cover a wide area in the fire and no repeats were performed. The desired experimental conditions for soot property measurements were not achieved in this test series. Although no significant quantitative results are available, the limited data provided an assessment of the overall operation of the diagnostic and indicated the soot optical diagnostic operated properly in these larger fires.

B. Test Matrix for December 2002 through January 2003

A second set of tests was performed in the winter of $2002 / 2003$ to collect a comprehensive set of TCRN measurements in the 2 m JP-8 pool fires at multiple locations in and over the fire. It was desirable to take a larger data set that would provide statistical confidence in the measured values of K_e with at least ten data points at each location (Coleman and Steele, 1999).

Measurement heights of 1 m, 2 m, 3 m, and overfire (i.e., in the chimney above the flame zones at about 6 m) were studied (see Table 4). These locations are needed to assess the use of a single extinction coefficient for all regions of the pool in FUEGO and VULCAN, and they were selected based upon input from code developers and users of FUEGO and VULCAN. The lower height of 1 m is located at the top of the vapor dome (i.e., 1/2 pan diameter); the 2 m location (1 pan diameter) is the necking region of the fire; the 3 m location (1 1/2 pan diameters) is in the highly puffing region; and the overfire region corresponds to all published data on soot optical properties in large fires. At the lowest height (1 m) the probe was approximately 30.5 cm (12 inches) off-center, and at all other heights it was located 10.2 cm (4 inches) from the center of the fuel pan. More than ten fire tests were performed at each measurement location, but only ten data points were included in the final analysis (eleven for overfire) after erroneous runs (from operator error, incorrect communication between staff in remote areas, etc.) were eliminated.

The centerline temperatures, pool heat flux, fuel recession, video coverage, air inlet characterization, amount of fuel, and burn duration were recorded for each test and are available upon request from the authors.

Table 4. Test locations in the 2 m pool fires.

1m (1/2D)

Index	Date	Location	Test
1	01/10/03	1m (1/2D)	T4
2	01/20/03	1m (1/2D)	T2
3	01/20/03	1m (1/2D)	T3
4	01/20/03	1m (1/2D)	T4
5	01/21/03	1m (1/2D)	T1
6	01/21/03	1m (1/2D)	T2
7	01/21/03	1m (1/2D)	T3
8	01/22/03	1m (1/2D)	T1
9	01/22/03	1m (1/2D)	T2
10	01/22/03	1m (1/2D)	T3

3m (1.5D)

Index	Date	Location	Test
1	12/10/02	3m (1.5D)	T1
2	12/10/02	3m (1.5D)	T2
3	12/10/02	3m (1.5D)	T3
4	12/10/02	3m (1.5D)	T4
5	12/10/02	3m (1.5D)	T5
6	1/8/03	3m (1.5D)	T1
7	1/8/03	3m (1.5D)	T2
8	1/8/03	3m (1.5D)	T3
9	1/8/03	3m (1.5D)	T4
10	1/9/03	3m (1.5D)	T1

2m (1D)

Index	Date	Location	Test
1	12/5/02	2m (1D)	T1
2	12/5/02	2m (1D)	T2
3	12/5/02	2m (1D)	T3
4	12/5/02	2m (1D)	T4
5	12/3/02	2m (1D)	T2
6	1/9/03	2m (1D)	T2
7	1/9/03	2m (1D)	T3
8	1/9/03	2m (1D)	T4
9	1/9/03	2m (1D)	T5
10	1/10/03	2m (1D)	T1

OVERFIRE

Index	Date	Location	Test
1	12/11/02	Overfire	T2
2	12/11/02	Overfire	T3
3	12/13/02	Overfire	T1
4	12/13/02	Overfire	T2
5	12/13/02	Overfire	T3
6	12/16/02	Overfire	T1
7	1/13/03	Overfire	T1
8	1/13/03	Overfire	T2
9	1/13/03	Overfire	T3
10	1/13/03	Overfire	T4
11	1/13/03	Overfire	T5

VIII. Results and Discussion

A. Soot Optical Properties Measurements

Calibration of the Soot Optical Properties Diagnostic

Calibration of the TCRN diagnostic was performed with polystyrene spheres of known density and optical properties similar to the previous work of Mulholland and Choi (1998). A latex microsphere suspension (5050A) was purchased from Duke Scientific Corporation with particles of 496 ± 3 nm diameter, a density of 1.05 g/cm^3, and refractive index of 1.59 at 589 nm (i.e., negligible imaginary component in the visible wavelengths). An aerosol of polystyrene microspheres was created using a Model 9302A atomizer aerosol generator and dryer from TSI, Inc. with a solution of 50 ml distilled water to 2 ml polystyrene suspension. Thermal tape was placed over a 15 inch section of plumbing following the dryer and maintained at 150°C to ensure no water vapor remained. Laser attenuations achieved with the low concentrations produced by the aerosol generator are on the order of 1-3%; therefore, a laser stabilizer was introduced for the calibration.

Figure 11 depicts the visible laser signal at 635 nm and the laser intensity output from the laser stabilizer during a 12 minute calibration period. The measured extinction coefficient of $K_e = 5.8$ is within 8.8% of the value of $K_e = 6.36$ predicted by Mie. Agreement between the theory and experiment to within 10% was an improvement over the past work of Mulholland and co-workers (Mulholland and Choi, 1998); however, better agreement by the same group of 4.0% was recently reported (Zhu, et al., 2000) for the specific extinction coefficient, $s = K_e/\rho\lambda$. It should be noted, however, that the signal-to-noise ratio at the low attenuation levels produced with the aerosol is much lower than in the fire tests. An attempt was made to use a fluidized bed to generate a higher-concentration calibration flow with higher signal to noise ratio; however, the available equipment was not capable of producing an aerosol with a stable, high-concentration output.

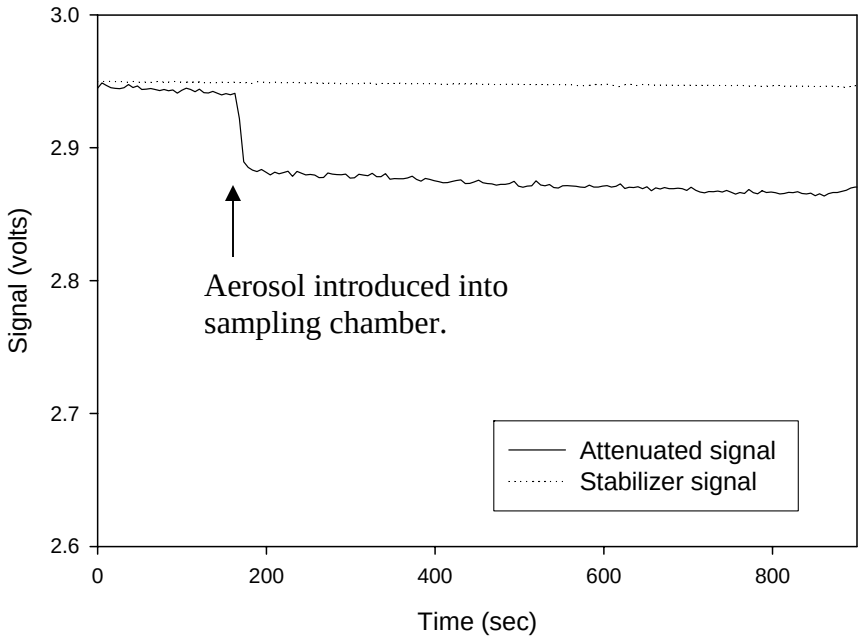

Figure 11. Visible laser signal at 635 nm during a 12 minute calibration test of the TCRN with polystyrene spheres of know optical properties. The dotted line is the output of the laser stabilizing unit.

Preservation of Soot Microstructure during Transport

In 2002, the soot sampler was used to obtain soot samples in the flame zone and in the transmission cell during a 0.3 m fire. The purpose of these samples was to compare the soot morphology to ensure that it was not altered in transport to the transmission cell. Representative TEM images of the soot from two sample locations are shown in Figure 12. The soot in all images can be described as near-spherical primary particles agglomerated into wispy chains.

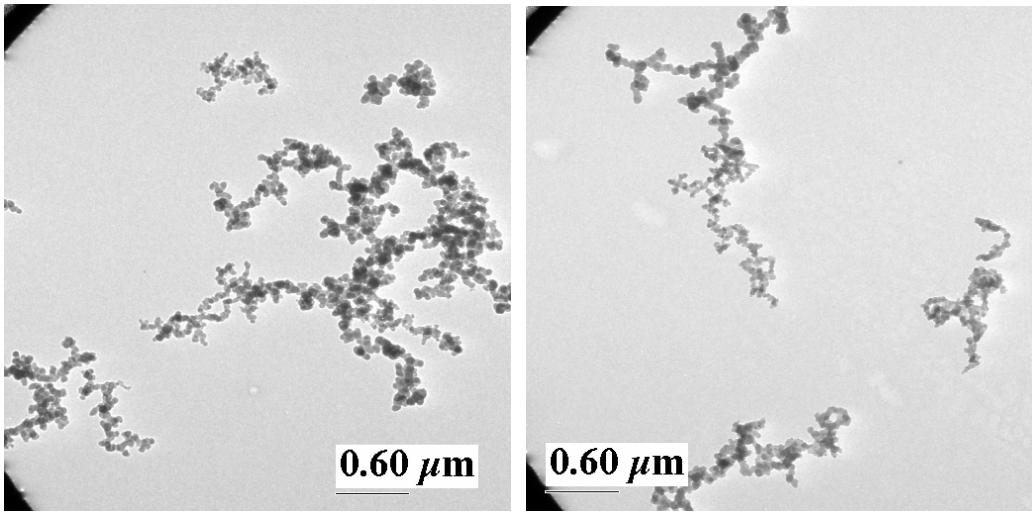

Figure 12. TEM images of soot from overfire and cell in a 30 cm JP-8 fire.

Upon observation of the images, it can be noted that transport through the lines to the transmission cell does not appear to have significantly altered the morphology of the soot (i.e. aggregated primaries existed in the cell). A quantitative analysis of the soot, as described previously, provides more evidence by comparing aggregate properties such as diameter of primaries (d_p), fractal dimension (D_f), and fractal prefactor (k_f). The primary particle sizes range from approximately 25-100 nm. The actual range of sizes varies from sample to sample, but the average primary particle diameter for all samples is approximately 50 nm.

In addition to analysis of the primary particle diameter, a quantitative assessment of the aggregate properties was performed. The aggregate properties of all samples were consistent. The quantities measured are also consistent with values reported in the literature. Typical values of D_f reported in the literature are 1.6-1.9, and typical values for k_f are 7.5-9.0. A summary of the morphological measurements is shown in Table 5. It can be concluded that the morphology of the soot is not altered in transport from the flame zone to the transmission cell; thus the optical property measurements can be made on soot transported to the cell with confidence that the measurements will be relevant in the flame zone. The experimental arrangement used for the 0.3 m fires is very similar to that used for the 2 m fires; therefore, the soot should not be altered in transport.

Table 5. Fractal properties of aggregates from the flame zone, overfire region, and in the transmission cell for 30 cm JP-8 pool fires.

JP8/Cases	D_f	k_f	d_p
Flame 1	1.58	8.60	50.9
Flame 2	1.61	8.54	45.2
Overfire 1	1.58	7.88	54.1
Overfire 2	1.64	7.92	54.3
Cell	1.63	8.07	50.5

Measurements in the Lab-Scale Santoro Burner

The Santoro burner is an ideal lab-scale comparison measurement for the diagnostic. Many studies over the past few decades have focused on characterizing the structure of an ethylene/air diffusion flame established using the Santoro burner, and several recent investigations published measurements of the dimensionless extinction coefficient and scattering albedo of soot aggregates for various fuels in the post-flame region of the burner (Mulholland and Choi, 1998; Zhu, et al., 2000).

Figure 13 shows the Santoro burner. The dimensionless extinction coefficient was measured in the post flame region of an over-ventilated ethylene/air diffusion flame established on the Santoro burner. The approximate settings for the burner operations were fuel and air flow rates of 0.37 and 42 SLPM, respectively. In the present work, average values of K_e of 8.33±0.48 and 8.32±0.64 at 635 nm and 1310 nm, respectively, were measured in the post flame region of an under-ventilated ethene flame. Mulholland and Choi (1998) reported a value of 8.50 m^2/g for the specific extinction coefficient of post-flame ethane soot on the same burner, which corresponds to a value of K_e=9.4±0.12 assuming a density of 1.74 g/cc for soot. The discrepancy in the measured and reported values of the dimensionless extinction coefficient may partly be attributed to differences in the flames established at different geographical elevations. In the study of Mulholland and Choi, the fuel and air flow rates were not reported for replication, and the atmospheric pressure was near sea level. The elevation of 1615 m (5300 ft) of Albuquerque is significantly higher, which causes the flames to widen from enhanced diffusion at lower pressures. Further measurements would be required to narrow the differences, which is beyond the scope and resources of the current study. The low standard deviations in the data give good confidence in the measured values.

Santoro Burner Ke values

		VIS	IR
5-28-B1	1	8.01	
	2	8.5	
	3	8.44	
5-28-B2	1	8.42	8.43
	2	8.51	8.54
	3	8.59	8.6
5-28-B3	1	8.03	7.89
	2	8.04	7.95
	3	8.17	8.15
	4	8.58	8.65
AVG		**8.33**	**8.32**
STD DEV		**0.24**	**0.32**

Figure 13. The Santoro burner with an (over-ventilated) ethylene/air diffusion flame and measured values of the dimensionless extinction coefficient of soot in the post flame region of an under-ventilated flame established on the same burner.

Measurements in a 2 m JP-8 Pool Fire

The dimensionless extinction coefficient of soot was measured during forty-one 2 m JP-8 pool fires in the FLAME facility. An illustration of the data and analysis for a single fire is presented before the complete results at all four heights.

Typical laser traces obtained at 2 m above the fuel surface for 635 nm (visible) and 1310 nm (infrared) wavelengths during a 2 m JP-8 fire are shown in Figure 14. Fourteen minutes of data are included in the graph (time, t, is shown on the horizontal axis), which is fairly representative of all tests, with t=0 coincident with ignition. The flames persist for up to 25 minutes, but the water below the fuel in the pan begins to boil somewhere between 13 and 15 minutes, making the fire burn unsteadily. Characteristic time periods during the fire are indicated by letters A, B, C, and D.

Period A is a preheat period that lasts for approximately 1 1/2 minutes while the fire is developing after ignition. During that time, hot soot and gas products are pulled through the TCRN plumbing to heat the lines. It was discovered, through trial and error, that consistent results were not obtained in the cold winter mornings and warm afternoons until this preheat was performed. After preheating the lines, the plumbing is purged with filtered air while a background laser signal is obtained during Period B.

At about three minutes after ignition, soot is again pulled through the (preheated) lines for one minute of Period C to allow transients to subside. Finally, the soot and gas

products are directed through the mass filter during Period D while the attenuated laser signals are recorded. Period D typically ranged from two to 3.5 minutes.

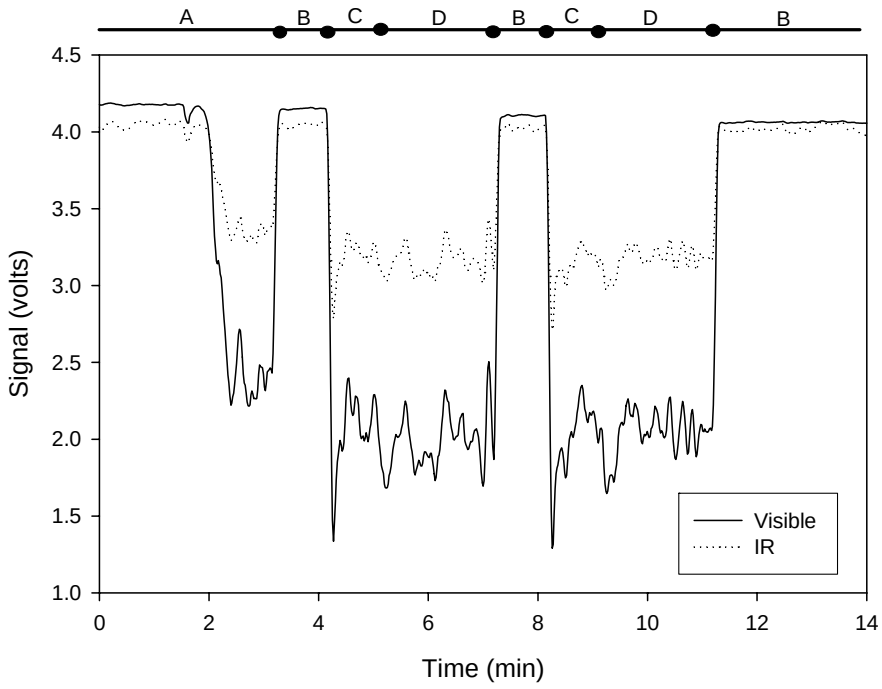

Figure 14. Typical laser traces at 2 m height above the fuel at 635 and 1310 nm during fourteen minutes from ignition of a 0.132 m^3 (35 gal), 2 m JP-8 pool fire.

Large fires are inherently unsteady in nature from the full-scale turbulent motions, and these fluctuations are reflected in the K_e data obtained. Repeatability of the diagnostic is therefore expected to be high during measurements of background laser attenuation, whereas signal variations are anticipated when soot is being sampled. Figure 15 demonstrates the repeatability of the visible and infrared laser signals of the TCRN during four fire tests where soot was sampled at 2 m above the fuel surface. The laser signal on both plots has been normalized from 0 to 1 so percentage attenuation can be readily compared. It is evident from these plots that the background laser signal remains constant at 100% throughout each test. In all four fires, a comparable attenuation of about 50% in the visible and 20% in the infrared signal is seen during the sampling period (Period D from Figure 14), although minor fire-to-fire fluctuations are present.

Equation 1 can be rearranged to determine the dimensionless extinction coefficient of soot, K_e, from the measured parameters,

$$K_e = -\ln(I/I_o)\lambda/f_v L\,, \tag{9}$$

where I/I_o is the ratio of attenuated to background laser signal (with and without soot), respectively, λ is the laser wavelength, and f_v is the volume fraction of soot measured over path length L.

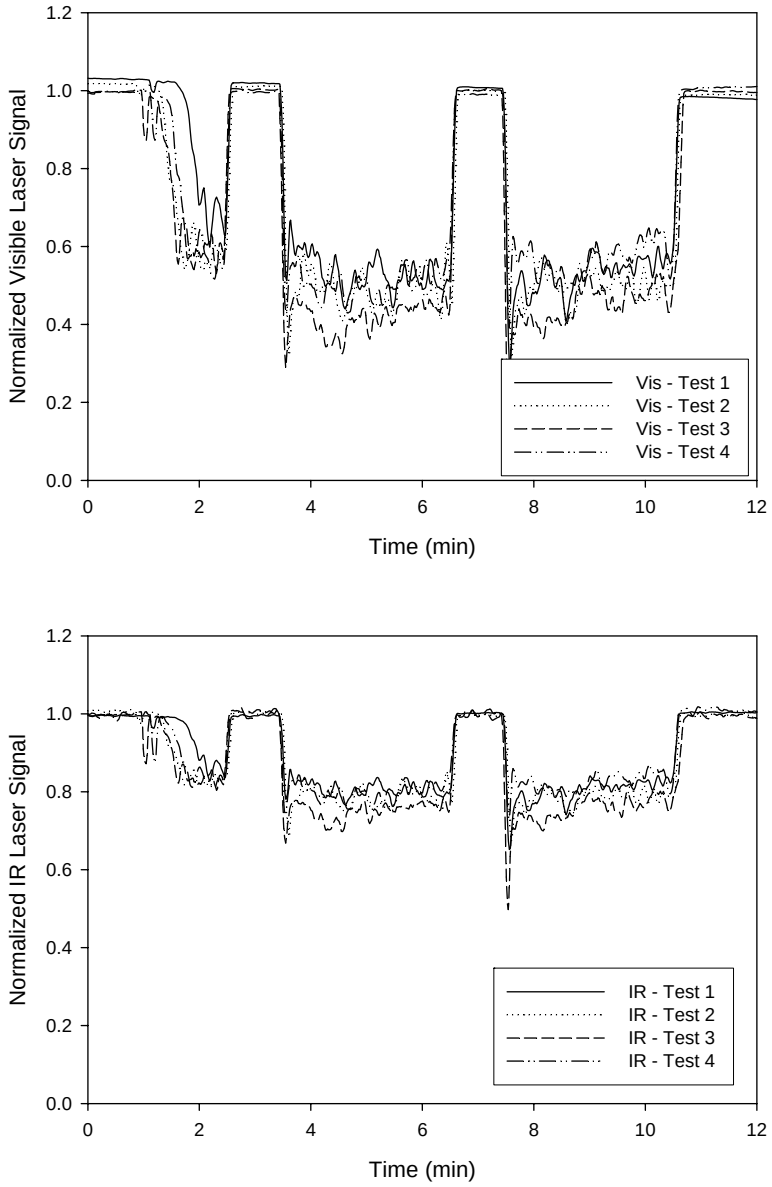

Figure 15. Normalized visible (upper) and infrared (lower) laser signals at 2 m height during four 2 m JP-8 pool fires showing good repeatability between runs.

The average soot volume fraction in the sampling chamber is calculated from a portion of the exit flow passed through a mass filter at a known rate. The expression for obtaining the volume fraction comes from its definition,

$$f_v = \frac{V_s}{\dot{V}\,\Delta t} = \frac{m_s/\rho_s}{\dot{V}\,\Delta t}, \tag{10}$$

where m_s is the mass of soot collected on the filter, ρ_s is its density, and $\dot{V}$ is the volumetric flow rate of the N_2-soot mixture through the filter, and Δt is the sampling duration.

The dimensionless extinction coefficient, K_e, obtained from the visible and infrared laser traces of the eight samples of Figure 15 (four fires with two sampling periods each) are shown in Figure 16. The corresponding values are tabulated below the graph. Two data points (a and b) from each fire test are indicated by the labels T1, T2, T3, and T4, respectively, corresponding to the value obtained from the first and second sampling period of the test.

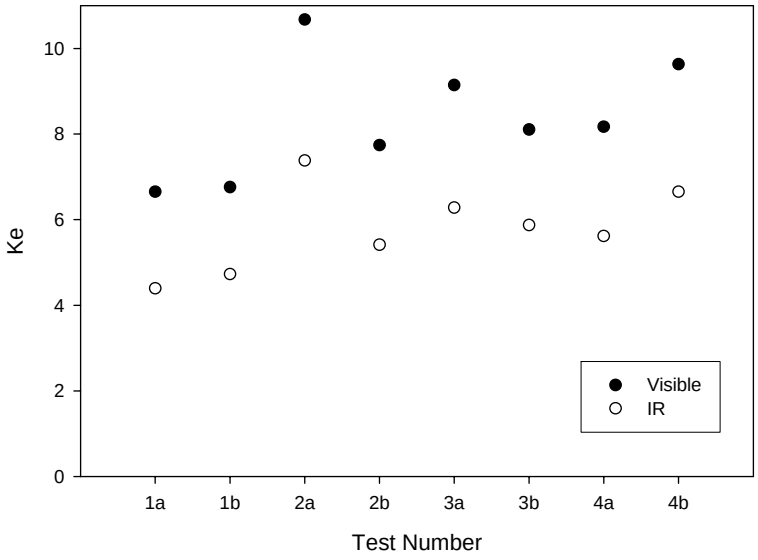

Test	Ke-Vis	Ke-IR
T1a	6.65	4.39
T1b	6.76	4.73
T2a	10.68	7.38
T2b	7.74	5.41
T3a	9.14	6.28
T3b	8.10	5.87
T4a	8.17	5.62
T4b	9.63	6.65

Figure 16. Dimensionless extinction coefficient from each sample of the four 2 m JP-8 pool fires on December 5, 2003 (2 m HAB).

It is evident from the extinction coefficients calculated from four fires under identical conditions that significant variation exists in results from each sampling period. One possible explanation could be changes in the environmental conditions between tests. During the winter days in Albuquerque, the mornings are very cold during test T1, slightly warmer by the time the second test T2 is performed mid-morning, and warming to a fairly constant temperature before and after noon for tests T3 and T4. However, after careful comparison of the tests shown in Figure 16 and those from other days, there does not appear to be a consistent trend between variations in the measured K_e values and the cooling / heating of the FLAME facility.

Another potential explanation for variation in the measured extinction coefficients from the fires established under identical conditions is the inherent fluctuations of the fires themselves. One way to address this concern is to consider whether longer time-averaging will have an effect on the variations in the results. Figure 17 shows four K_e values calculated from the same fires of Figure 15 and 16, but this time both samples from each fire are combined in the analysis. The mass of soot obtained from each sample during Period D is totaled when calculating the average volume fraction, and the average laser attenuation during both samples is used for solving for the extinction coefficient.

Longer time averaging over all samples on a per-fire basis reduced the variation in the K_e results. It should be mentioned that the choice to average across the samples in each fire was based on more than the desire for reducing the standard deviation. Averaging over different periods during the fires ensures each average value includes effects which may be due to different periods in the fire, whether introduced naturally or by the FLAME facility. It also worth noting that performing both analysis methods on all the data resulted in a nearly identical average K_e value (within 1%) at each measurement location with a reduction in the standard deviation by a factor of two using the longer temporal averaging technique.

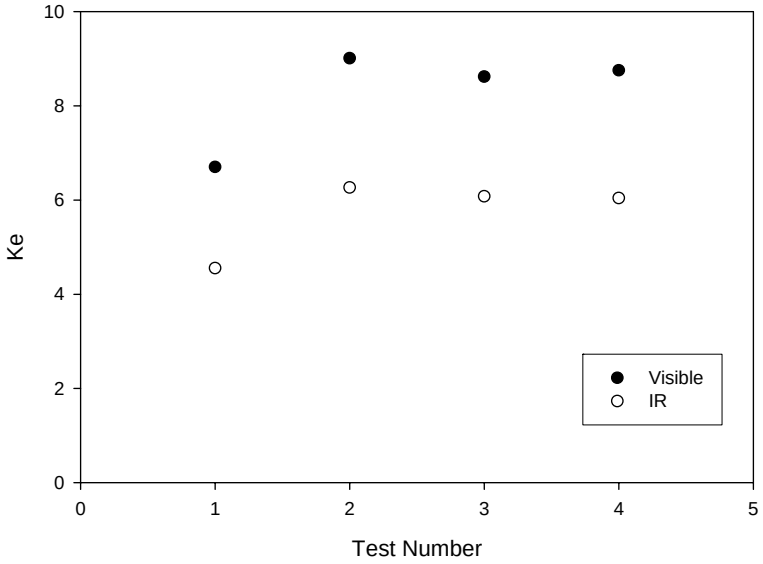

Test	Ke-Vis	Ke-IR
T1	6.70	4.55
T2	9.01	6.26
T3	8.62	6.08
T4	8.75	6.04

Figure 17. Dimensionless extinction coefficient from averaging the samples of the four 2 m JP-8 pool fires on December 5, 2003.

Figure 18 shows the average measured dimensionless extinction coefficient, K_e, obtained from ten fires at each location in FLAME of 1 m, 2 m, 3 m, and overfire (shown at about 6 m) for laser wavelengths of (a) 635 nm and (b) 1310 nm. The average value of K_e at each height is indicated by the sphere and the error bars include two standard deviations for 95% confidence in the reported values. Both the average and standard deviation at each height are tabulated below the figure.

Recent measurements of K_e in the overfire region of lab-scale and turbulent fires have reported values in the range of 8.0-10.0 in the visible and infrared for ethylene and acetylene. The measured average overfire values of 8.4 and 8.7 at 635 nm and 1310 nm, respectively, are in excellent agreement with these reports. Despite the agreement in the post flame zone, caution must be used in generalizing the same conclusion to in-fire results at 1 m, 2 m, and 3 m locations. For the visible wavelength, there was little variation in the average K_e value with height in the fire. The K_e values for 1310 nm, however, were not as constant, varying from as low as 6.7 to as high as 8.7. The 95% confidence levels overlap around a value of approximately 8.0, suggesting that K_e may be constant in the infrared within the uncertainty of the measurement.

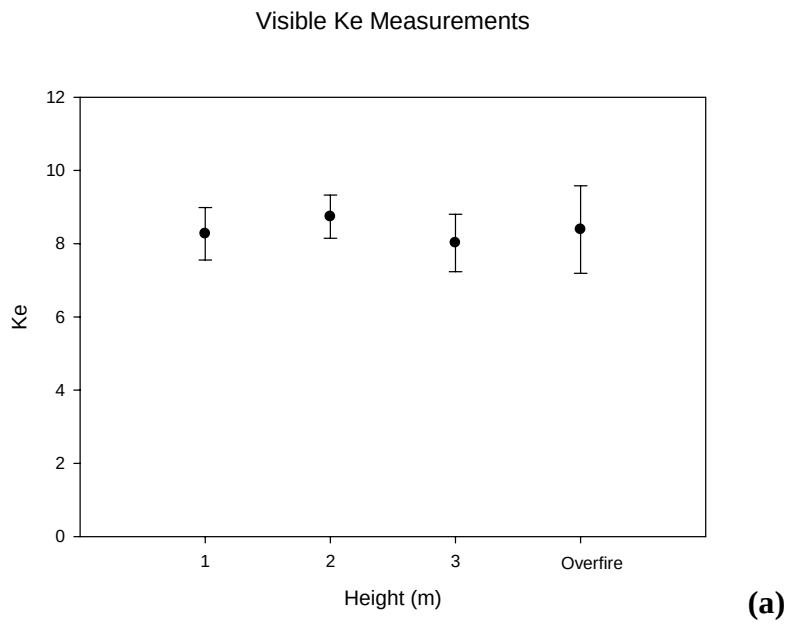

(a)

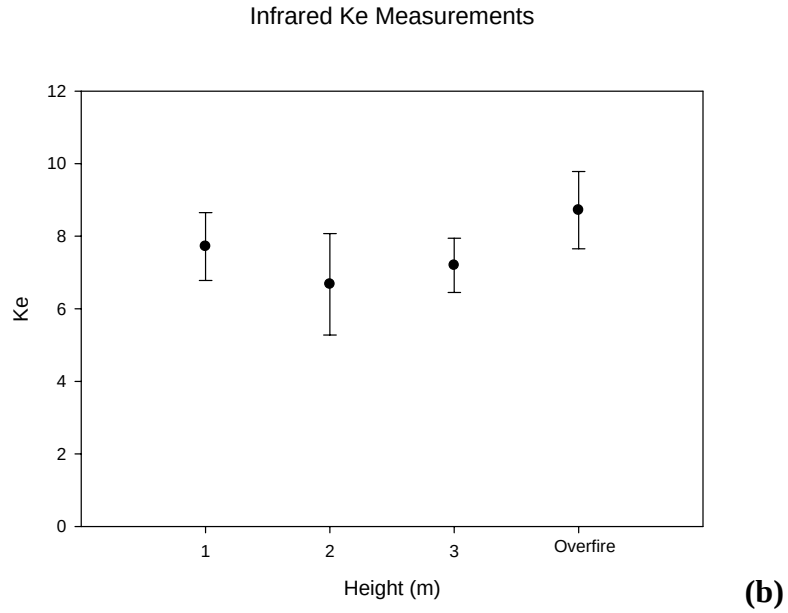

(b)

HAB (m)	Visible	Infrared
1	8.3 ± 0.36	7.7 ± 0.47
2	8.7 ± 0.30	6.7 ± 0.70
3	8.0 ± 0.39	7.2 ± 0.38
Overfire	8.4 ± 0.60	8.7 ± 0.53

Figure 18. Dimensionless extinction coefficient for ten tests at each of four locations in the 2 m JP-8 pool fire of the FLAME facility at (a) 635 nm and (b) 1310 nm.

B. Soot Morphology Measurements

Thermophoretically sampled soot was obtained two minutes after ignition during a select number of fires at each measurement location (see Figure 2) while performing the optical probe tests. A minimum of three samples were captured at each location with good coverage of soot aggregates. Images of approximately 60 aggregates were then obtained via TEM on the set of grids at each height.

Figure 19 shows soot aggregate images obtained at heights of 1 m, 2 m, 3 m, and the overfire region of the 2 m JP-8 pool fires. Portions of two aggregate images found at each location during different fire tests are presented. Typical wispy, chain-like aggregates with a uniform primary particle diameter were observed at each location, although, as can be seen in the second image at 2 m height, variation of primary particle sizes is observed from aggregate to aggregate. It should be noted that the images presented were obtained at fairly high magnification to see details of the individual particles within the aggregates, but they were not used to study the fractal properties of entire aggregates. Images obtained with lower magnifications were used for this purpose.

Custom imaging software (shown previously in Figure 6) was written to determine the radius of gyration, R_g, fractal dimension, D_f, and prefactor, k_f, from each aggregate image. A user–specified graylevel value (0=black to 255=white) defines the background light intensity, and the program isolates the aggregate pixel by pixel in grayscale color space relative to this threshold. All pixels darker than the threshold value (i.e., with lower graylevel) are considered part of the aggregate, and the rest are considered background. The background pixels are set to a continuous color (green in the screen shot) to allow the user to see that an appropriate value has been set. Through trial and error, the threshold value is adjusted up and down by one to five graylevel to witness changes in the perimeter pixels of the soot primaries. Additionally, a special edge detection routine enables the program to automatically highlight edge pixels, which also helps the user judge that an appropriate threshold has been specified. Analysis of the fractal properties of the aggregate are then performed on a per-pixel level (Manzello and Choi, 2002; Choi, 2002); that is, instead of trying to identify each soot primary particle, each pixel is considered its own primary particle.

The number of primaries (i.e., pixels), N, is simply the number of pixels below the threshold graylevel. The radius of gyration, R_g, is easily obtained from Equation 3 after the centroid is determined. Next, the projected aggregate area, A_a, is found by multiplying N by the physical size represented by the pixel determined from the tick mark imprinted by the electron microscope. Equation 4 is then used to empirically calculate the surface area of the aggregate, A_a, in three-dimensional space.

To determine the fractal dimensions of the aggregate using Equation 5, the diameter of the primary particle is required. The custom software allows the user to select multiple primary particles in the image and calculate the average diameter, d_p. This single value of d_p from the aggregate is insufficient to solve for both k_f and D_f from Equation 5; therefore, a special feature was added to the software to simplify calculation of the fractal

dimension and prefactor retroactively from a collection of saved aggregate analysis files. The user specifies which previously-analyzed aggregates to consider, and the software tabulates the values of N, R_g , d_p , log(N), and log(R_g/d_p). Microsoft Excel then loads the data and fits a line to it in the form of Equation 6 to determine a single value of k_f and D_f at each height from the 60 aggregate images.

Plots of R_g and d_p at heights of 2 m, 3 m, and overfire are given in Figure 20, and the logarithmic fits to Equation 5 to obtain k_f and D_f are shown in Figure 21. Morphology results are also tabulated at the bottom of Figure 21 for all four heights. The analysis for 1 m height was performed on TEM negatives scanned for analysis which had considerably less contrast than images directly downloaded from the electron microscope at the other heights. Additionally, the negatives did not have a corresponding physical scale factor to calculate the radius of gyration and primary particle diameter. However, it is still possible to calculate the fractal quantities which include only ratios of dimensions. From observation of images at the same scale (e.g., Figure 19), the primary particles at the 1 m height have smaller diameters than those at the greater heights.

From Figure 20 it is seen that the average radius of gyration and primary diameter are smallest at the 3 m height (not considering the 1 m height). In addition, these quantities are larger at 2 m in the necking region of the fire than at the overfire location where the soot may be most mature prior to oxidation higher in the fire. Another general observation comes from review of the large collection of images. Additionally, aggregates at the overfire location tend to appear the most uniform from sample to sample with radius of gyration and particle size that appear similar to the naked eye.

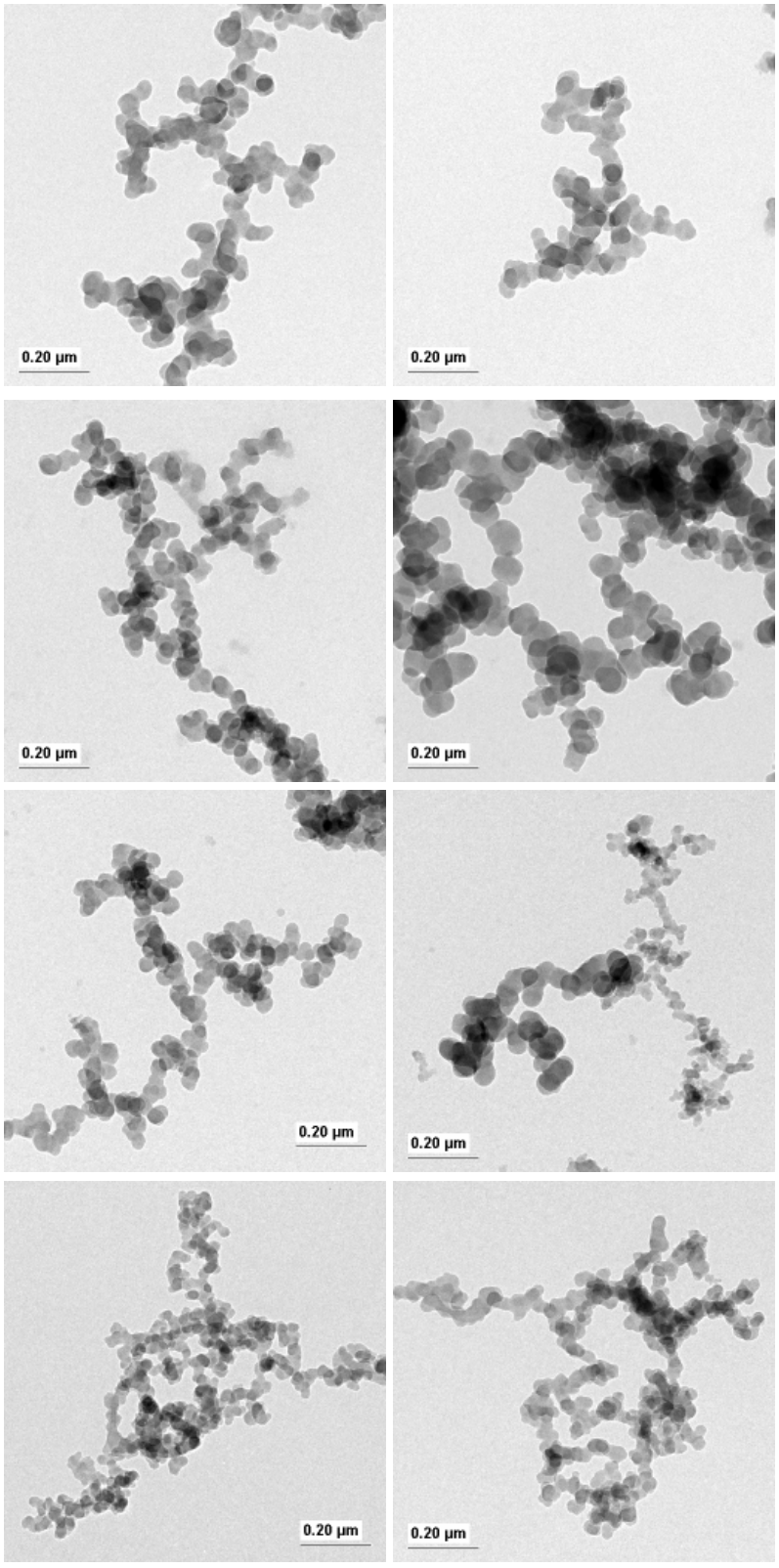

Figure 19. Soot aggregates at heights of 1 m, 2 m, 3 m, and overfire in the 2 m JP-8 pool fires.

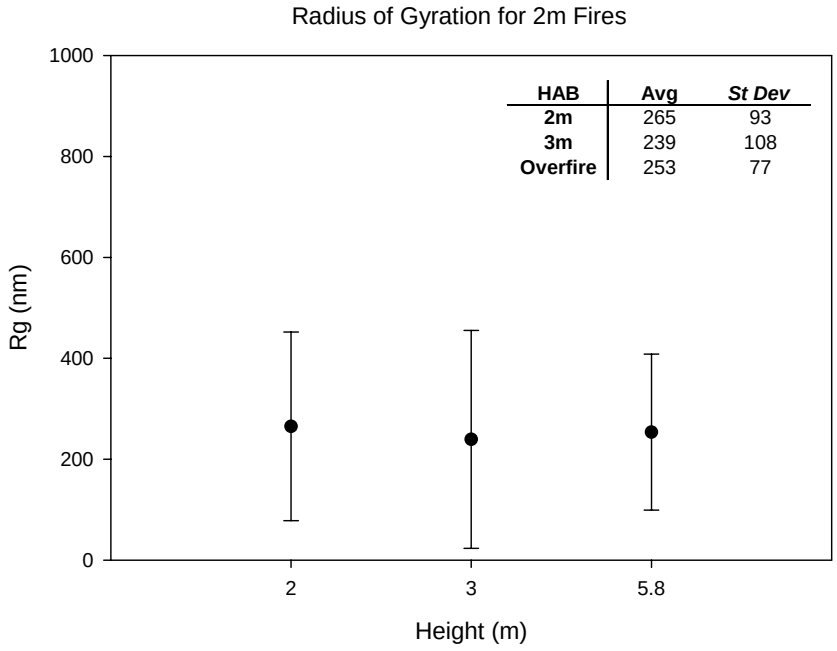

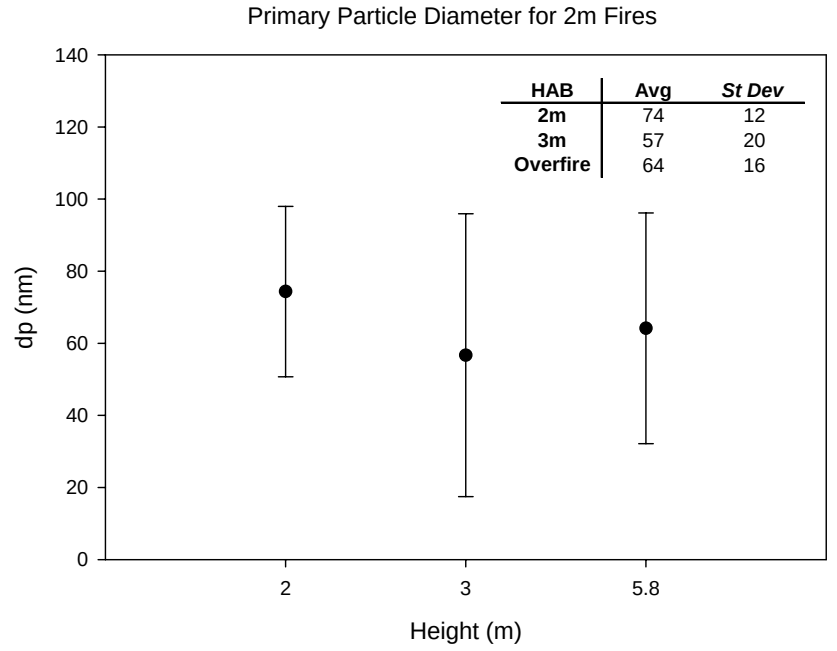

Figure 20. Primary particle diameter and aggregate radius of gyration measurements at heights of 2 m, 3 m, and overfire in the 2 m JP-8 pool fires.

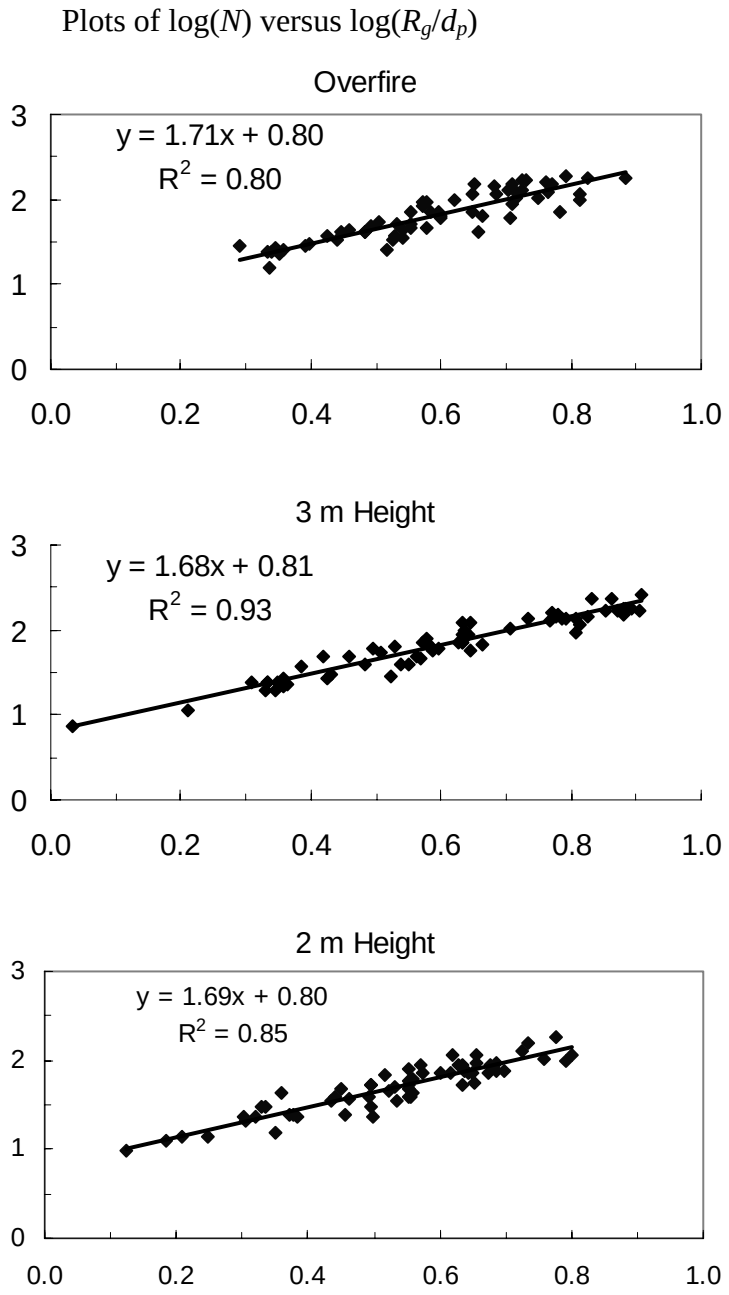

Height	# Aggs.	R_g (nm)	σR_g	d_p (nm)	σd_p	k_f	D_f	Intrcpt.	Slope	Corr. R^2
Overfire	63	253.5	77.3	64.1	16.0	*6.31*	*1.71*	0.800	1.71	0.80
3 m	63	239.2	108.0	56.7	19.6	*6.39*	*1.68*	0.806	1.68	0.93
2 m	61	264.9	93.5	74.3	11.8	*6.26*	*1.69*	0.797	1.69	0.85
1 m	23	- -	- -	- -	- -	*6.20*	*1.72*	0.793	1.72	0.84

Figure 21. Logarithmic plots used to determine the fractal dimensions from a set of aggregate images using custom software and the relation in Equation 6.

High-Resolution Transmission Electron Microscope Analysis

Soot TEM samples from each location (see Figure 2) were sent to Dr. Randall L. Vander Wal of the National Center for Microgravity Research Center at NASA Glenn Research Center. An initial high-resolution TEM (HRTEM) analysis was performed to assess whether to pursue further analysis with a fringe analysis technique (Vander Wal and Tomasek, 2003). This section summarizes his findings.

Figures 22, 22, 24, and 25 contain both standard and high-resolution TEM images of the samples collected at 1 m, 2 m, 3 m, and overfire locations, respectively. The following quote contains Dr. Vander Wal's observations:

"As an overview, we saw a modest increase in the graphitic structure of the soot with increasing height, or residence time. There also appeared to be a significant change in the aggregate morphology. 'Normal' branched aggregates were observed at the lowest height, but not higher. As you will see, the higher positions led to a major increase in the connectivity of the aggregate (though the fractal dimension would never reveal this). The aggregate increasingly became 'filled in'. To me, this illustrates the predominance of continued mass growth subsequent to aggregation. Beyond this, we did not pursue imaging on the 'aggregate/primary particle level'. As you will see, the nanostructure did increase with increasing height, but the 'core' nanostructure was largely preserved, reflecting both its inception origins and an absence of high temperature exposure. Notably with increasing radial distance (outward), there appears to be more nanostructure, i.e., the soot appears to have larger, longer carbon layer planes, compared to the interior. This is to some degree a function of the imaging and radial depth and curvature of the particle, but there is sufficient difference based on our experience to say that there is more than what would be expected based on a spherical primary particle. This may speak to different growth species at the higher heights and/or the (likely) higher temperature (a synergy most likely)."

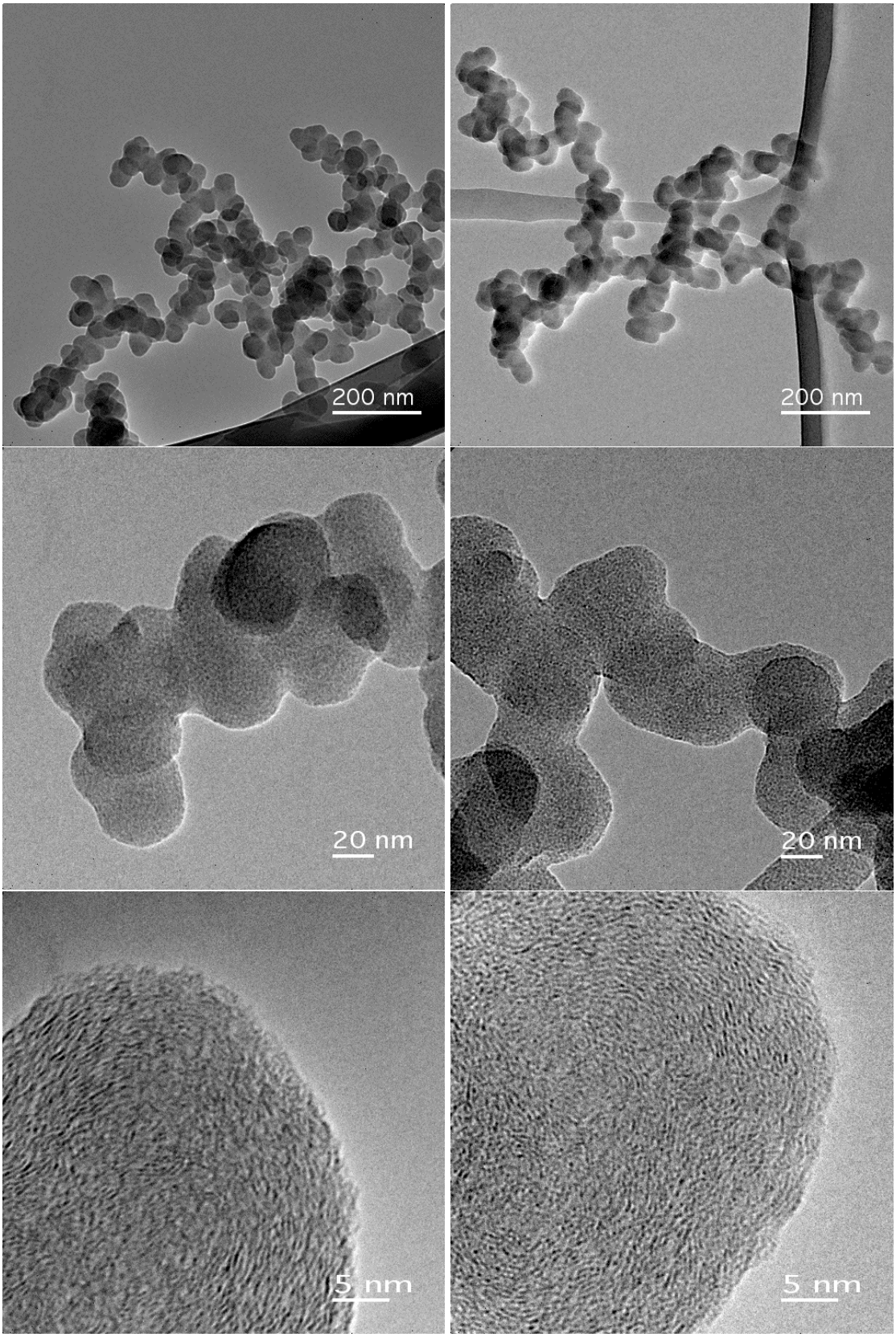

Figure 22. TEM images of soot from 1 m height in the 2 m JP-8 pool fires.

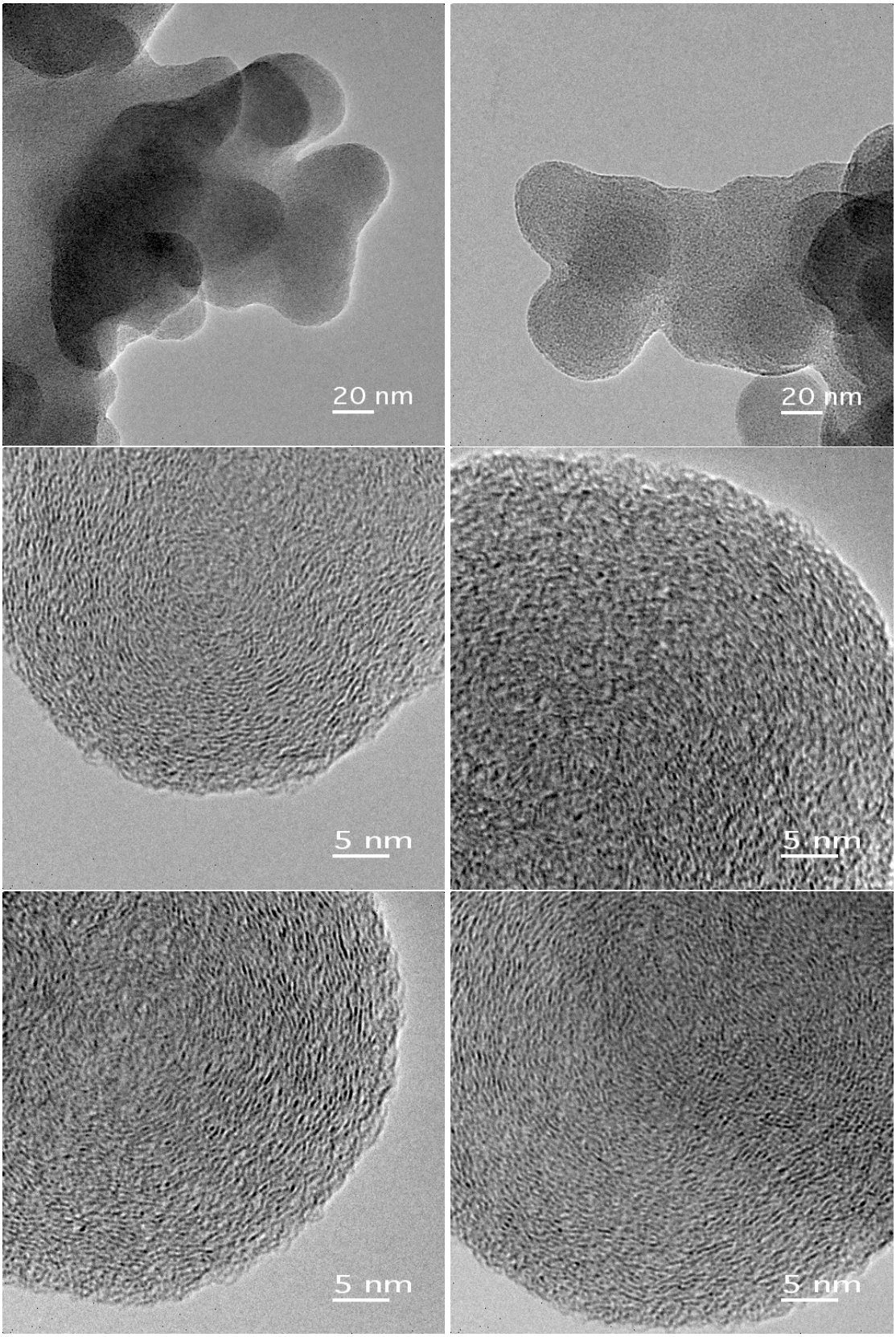

Figure 23. TEM images of soot from 2 m height in the 2 m JP-8 pool fires.

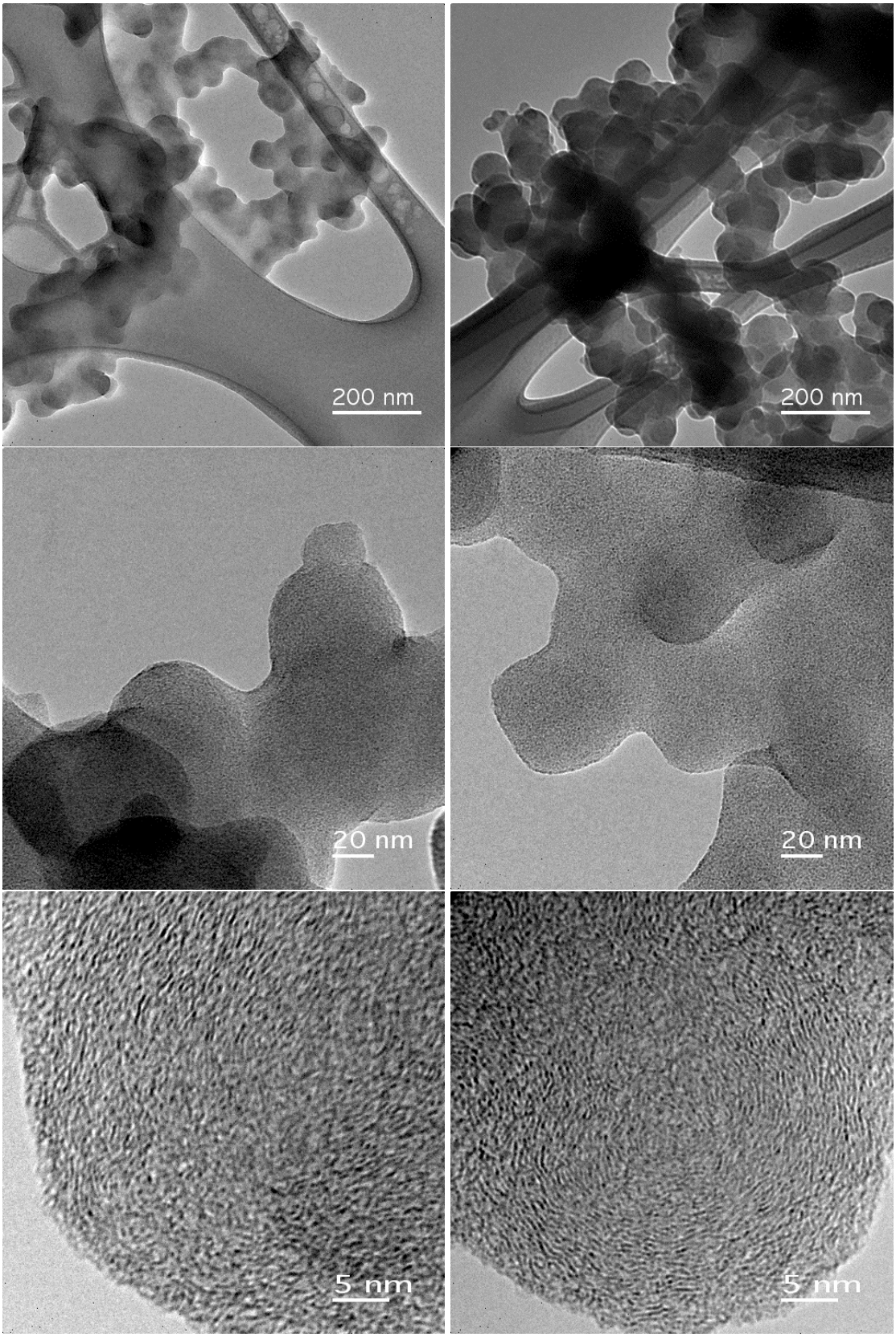

Figure 24. TEM images of soot from 3 m height in the 2 m JP-8 pool fires.

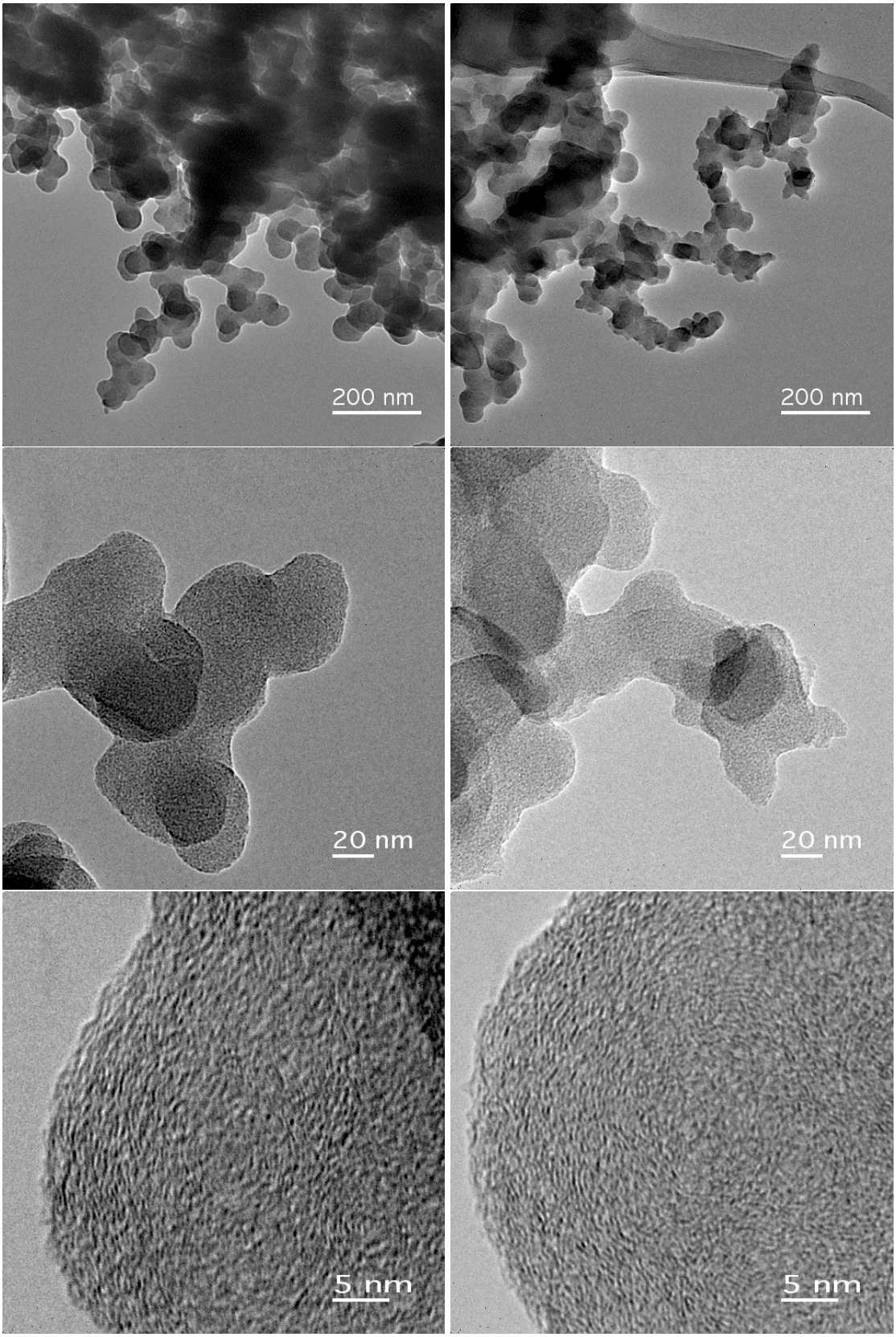

Figure 25. TEM images of soot from the overfire location in the 2 m JP-8 pool fires.

Aggregates with Two Primary Particle Sizes

One intriguing discovery of this study was the presence of aggregates which appear to consist of a traditional wispy chain of edge-connected particles of the same diameter augmented with random smaller particles of a common diameter. Figures 25a and 25b show samples of such aggregates obtained at 1 m and 2 m heights, respectively. Similar aggregates were found at all locations in the fire. In all cases, the "normal" aggregate consists of a larger particle diameter.

One potential explanation for these aggregates is that they are caused by the turbulent mixing of the fire. Mature aggregates formed at one location in the fire are transported by momentum processes through flame zones that are starting to form soot particles and/or continue the coagulation/agglomeration processes typically witnessed in lab-scale flames such as the Santoro burner. The larger aggregate passing through this region provides an attractive site for the smaller particles to coagulate or agglomerate, thus sticking to the outer portions of the structure.

These "mixed aggregates" were witnessed at all locations sampled in the 2 m pool fires, and increased in quantity with height. From a scan of approximately 100 aggregates at each height it is estimated that approximately 10% of aggregates at the overfire location included mixed sizes.

The effect of these mixed aggregates on the radiative emission from soot in large fires warrants further investigation. The traditionally accepted theories for scattering and absorption by particles are not applicable to these morphologies. For example, Mie scattering applies to isolated spherical particles and the Rayleigh-Debye-Gans theory accounts for a single particle diameter per fractal aggregate.

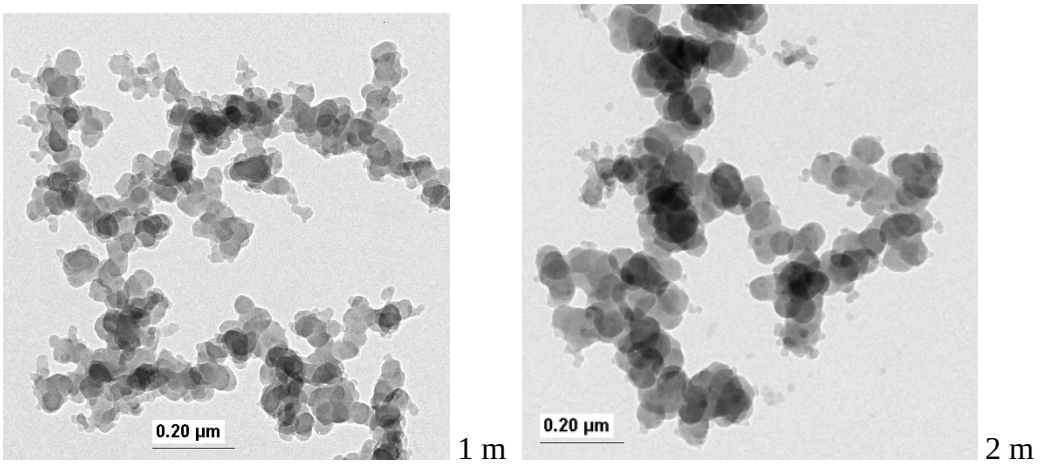

Figure 26. TEM images of soot showing mixed aggregates.

C. Comparison to Rayleigh-Debye-Gans Theory of Scattering

Based on the morphology of the soot, the optical properties can be calculated. The total extinction consists of two components, the portion of the light being absorbed and the portion of the light being scattered,

$$\sigma_{ext} = \sigma_{abs} + \sigma_{scat} \tag{11}$$

The relation of the mass specific extinction coefficient (σ_{ext}) to the light extinction coefficient (K in units of m^{-1}) and the dimensionless extinction coefficient (K_e) is

$$\sigma_{ext} = \frac{K}{M_s} = \frac{K_e f_v}{M_s \lambda} = \frac{K_e}{\rho_{soot} \lambda}, \tag{12}$$

where M_s is the mass concentration of smoke in kg/m^3.

The following section characterizes the extinction properties, scattering and absorption, based on the morphology of the soot collected in the 2 m JP-8 fires. The theory selected to calculate the extinction properties is dependent on the size parameter, x, which is based on the size of the particle, d_p, and the wavelength, λ. The size parameter is defined as (Bohren and Huffman, 1983)

$$x = \frac{\pi d_p}{\lambda}. \tag{13}$$

For small particles where $x<<1$, scattering can often be neglected leading to the Rayleigh limit solution of the Mie theory. This assumption is commonly used for simplicity when dealing with soot calculations and/or measurements, although aggregation of the primaries typically causes this assumption to result in underestimation of the extinction by approximately 30% (Faeth and Köylü , 1995 and Choi, et al., 1995). For particles of size similar in magnitude to the wavelength of energy, $x=O(1)$, the extinction properties of round particles can be described by the complex Mie theory (Bohren and Huffman, 1983). For large particles, $x>>1$, the extinction properties are calculated using geometric optics where the surface of the particle is treated as a normal surface.

Actual soot does not fit into any of these three categories very well. As stated before, aggregated soot particles are not likely within the Rayleigh regime for light in the visible or near-IR. There have been attempts to find the optical properties of soot using Mie theory by concentrating the entire mass of the soot agglomerate into an equivalent sphere, but this is not a good representation of a wispy chain (Köylü and Faeth, 1993). Since soot is a fractal aggregate, the Rayleigh-Debye-Gans theory for polydisperse fractal aggregates (RDG-PFA) was developed to calculate its scattering and absorption properties. In using this theory, several assumptions about the properties of the soot are invoked, i.e., the soot consists of fractal aggregates, which obey the power law relation between number of primaries and radius of gyration (see Equation 5); soot consists of spherical primary particles that just touch each other; and the index of refraction is

uniform (Faeth and Köylü, 1995). As shown in the previous two sections, the majority of aggregates contain a single primary particle size, and at higher imaging resolutions significant merging of the particles is apparent (see Figs. 19 and 22-25). Similar merging of the primary particles has been described by Faeth and coworkers (1995) for soot aggregates from the overfire region of turbulent flames, but it was shown that predictions of angular scattering by the RDG-PFA theory were reasonably accurate.

Equations 14 and 15 for the mass specific coefficients were derived from the total scattering and absorption cross sections (Köylü and Faeth, 1993). The resulting equations were compared to the same derivation performed in a later paper (Dobbins, et al., 1994), where it was determined that a typographical error existed. The sign of the exponent in the scattering term in the following equations has been corrected (positive value). The following equations display the derived expressions for the absorption and scattering properties of the soot as a function of their morphology.

Thus,

$$\sigma_{abs} = \frac{6\pi E(m)}{\lambda \rho_p} \tag{14}$$

and

$$\sigma_{scat} = \frac{4\pi x_p^3 k_f F(m)}{\lambda \rho_p} \left(\frac{3D_f}{16 x_p^2} \right)^{\frac{D_f}{2}} . \tag{15}$$

Here, *E(m)* and *F(m)* are functions of the complex index of refraction of the soot. The complex index of refraction is defined as $m=n-ik$, where n is the ratio of the speed of electromagnetic radiation in a vacuum to the speed in the medium. For absorbing media (such as soot), the index of refraction is always complex and the imaginary component is an indication of the absorptive property of the medium. The complex index of refraction for soot that will be used in all subsequent calculations is the one most frequently used, $m=1.57-i0.56$ (Smyth and Shaddix, 1996). The functions, E and F, of the complex index of refraction used in calculating the extinction are

$$E(m) = Im\left(\frac{m^2 - 1}{m^2 + 2} \right) \tag{16}$$

and

$$F(m) = \left| \frac{m^2 - 1}{m^2 + 2} \right|^2 . \tag{17}$$

The above equations for *E(m)* and *F(m)* can be used for $x<0.1$, but for shorter wavelengths or larger primary particles, up to $x \approx 0.5$, *E(m)* should be replaced by *E'(m)*, defined as

$$E'(m) = E(m) + \mathrm{Im}\left[\frac{x_p^2}{15}\left(\frac{m^2-1}{m^2+2}\right)^2\left(\frac{m^4+27m^2+38}{2m^2+3}\right)\right]. \qquad (18)$$

The above equations (14 through 18) were used to calculate the optical properties (primary interest was K_e) using only the soot morphology for comparison with the value of K_e measured using the TCRN diagnostic.

Figure 27 shows the soot optical properties calculated using the Rayleigh-Debye-Gans theory of scattering from Equations 14-18. The measured morphological properties d_p, k_f, and D_f , and two commonly accepted values of the refractive index of soot of m=1.57-i0.56 (Dalzell and Sarofim) and m=1.90-i0.55 (Lee and Tien) were used in the calculations. Considering first the most commonly reported refractive index of m=1.57-i0.56, the theory predicts K_e varies between 6.4-7.1 compared to measured values averaging near 8.5. The theory underpredicts the K_e value although the trend in K_e as a function of height is similar to the measurements. A similar pattern is seen for the infrared wavelength. RGD theory predicts K_e varies between 5.4-5.7 at 1310 nm, as opposed to measured values from high 7's to low 8's. Using the second value for the complex index of refraction, m=1.90-i0.55, only leads to further underprediction by the theory, thus reinforcing the need for accurate measurement of soot optical properties.

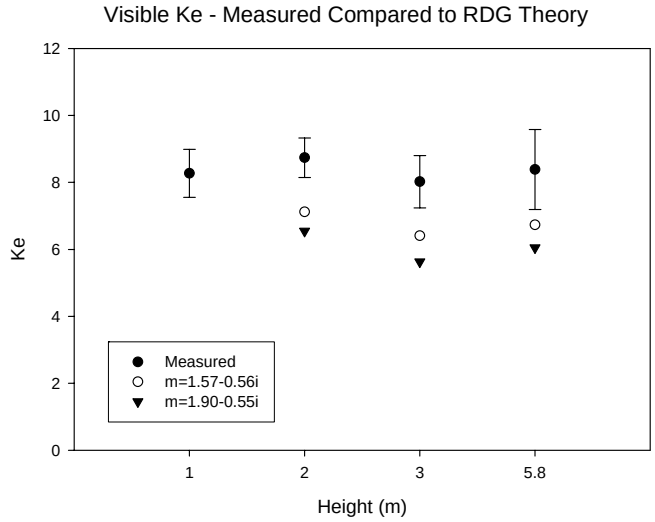

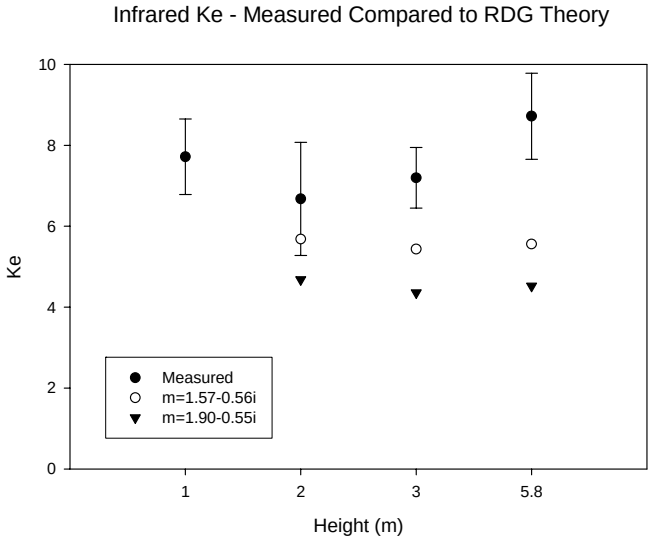

Wavelength: λ=635 nm

	d_p (nm)	k_f	D_f	Ke_{ext}
	m=1.57-i0.56 (Dalzell&Sarofim)			
2m HAB	74.3	6.26	1.69	**7.1**
3m HAB	56.7	6.39	1.68	**6.4**
overfire	64.1	6.31	1.71	**6.7**
	m=1.90-i0.55 (Lee&Tien)			
2m HAB	74.3	6.26	1.69	**6.5**
3m HAB	56.7	6.39	1.68	**5.6**
overfire	64.1	6.31	1.71	**6.0**

Wavelength: λ=1310 nm

	d_p (nm)	k_f	D_f	Ke_{ext}
	m=1.57-i0.56 (Dalzell&Sarofim)			
2m HAB	74.3	6.26	1.69	**5.7**
3m HAB	56.7	6.39	1.68	**5.4**
overfire	64.1	6.31	1.71	**5.6**
	m=1.90-i0.55 (Lee&Tien)			
2m HAB	74.3	6.26	1.69	**4.7**
3m HAB	56.7	6.39	1.68	**4.4**
overfire	64.1	6.31	1.71	**4.5**

Figure 27. Comparison of experimental dimensionless extinction coefficient values of soot to predictions of the Rayleigh-Debye-Gans theory of scattering using the measured soot morphology from the 2 m JP-8 pool fires.

D. Soot Composition Measurements

Carbon to Hydrogen Ratio

Soot samples were obtained at various heights above the fuel surface to monitor the change in carbon to hydrogen ratio. Sampling points were located 1 m, 2 m, 3 m, and overfire regions (~5-6 m) of a 2 m JP-8 pool fire. The results, including the average and standard deviation, are summarized in Table 6. A plot of C/H ratio as a function of height above the burner is shown in Figure 28. The vertical bar on each data point shows the standard deviation. Horizontal lines mark the C/H ratios associated with single precursor particles (1.75, 1.82, and 1.84) and with slightly carbonized aggregates (5.17 and 5.94) along the centerline of the normal ethylene diffusion flames examined by Dobbins and coworkers (1998). At least four different samples from each height were analyzed to produce the results.

Table 6. Carbon to hydrogen ratios.

Height (m)	C/H Ratio	Standard Deviation
1	8.3	2.9
2	3.9	0.4
4	5.7	1.5
6	7.8	1.8

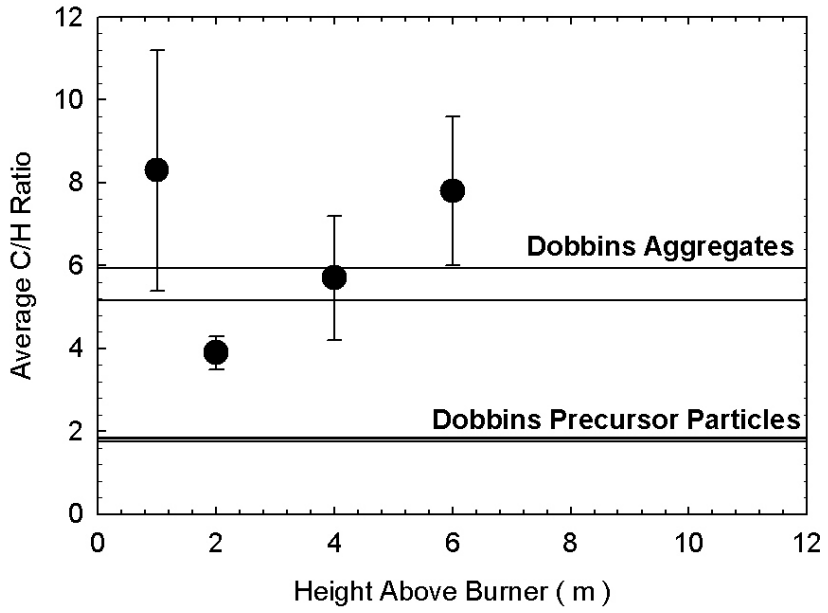

Figure 28. Carbon to hydrogen ratios of soot collected from JP-8 pool fires.

An interesting finding is that the lowest point in the flame zone has the highest C/H ratio. This could be because soot sampling was performed away from the centerline at this height. Attempts to sample at the centerline were complicated by an abundance of very sticky "soot" in the sampling region. The presence of this sticky "soot" reduced the ability to obtain repeatable laser signals for the soot optical measurements; therefore, the sampling point was moved to 30 cm (12 inches) off the centerline. The stickiness indicates a high organic content. It is likely that the sticky substance had a low C/H ratio, but it could not be measured. It is possible that the soot at the radial location of 30 cm experienced a different history than the centerline soot. Carbonization could have been caused by passage of the soot through a high temperature region. The existence of such a region away from the centerline at low heights is probable; a relatively cool, fuel-rich region is known to exist near the fire core.

The lowest C/H ratio, 3.9, was observed at 2 m above the fuel surface. Downstream of 2 m, the C/H ratio increases as the distance from the fuel pan increases. All of the soot C/H ratios measured in the JP-8 pool fires are greater than those of unagglomerated precursor particles, and are closer to those of the aggregates than to those of the precursor particles. The soot measurements at the 1 m location had the most variability, making it difficult to draw conclusions from the limited number of data points.

To the authors' knowledge, these measurements represent the first characterization of soot C/H ratio within the flame zone of large pool fires.

PAH Concentrations

For PAH analysis, six, five, twelve, and six samples were analyzed for 1 m, 2 m, 3 m, and overfire heights, respectively. Results from all of the samples are shown in Figure 29 to demonstrate the high variability in this type of measurement. Note that the abscissa of the graph corresponding to a height of 3 m has a range five times larger than those of the other graphs. If a PAH concentration is below the detectable limit, it is not shown. Similar to experiments conducted by Blevins, et al. (2002), the temperature of the sampling line was uncontrolled. The collected sample may contain particles and condensed gases. It is noted that the lighter gases have a greater probability of passing through the filter, while the heavier gases are more likely to condense and deposit on the filter. Thus, the amount of measurement-to-measurement variation caused by the uncontrolled filter temperatures decreases as the size of the molecule increases (Blevins, et al., 2002). As a result, the concentrations of the four- and five- ring molecules (202 g/mol to 252 g/mol in the present study) are expected to be more reliable than those for two- and three-ring PAH (128 g/mol to 178 g/mol presently). Compounds with molecular weights of 178 g/mol and above are the primary components in the samples collected 1 m from the fuel pan and in the overfire region. In contrast, all 14 targeted PAH are generally present in the samples collected 2 m and 3 m above the fuel pan.

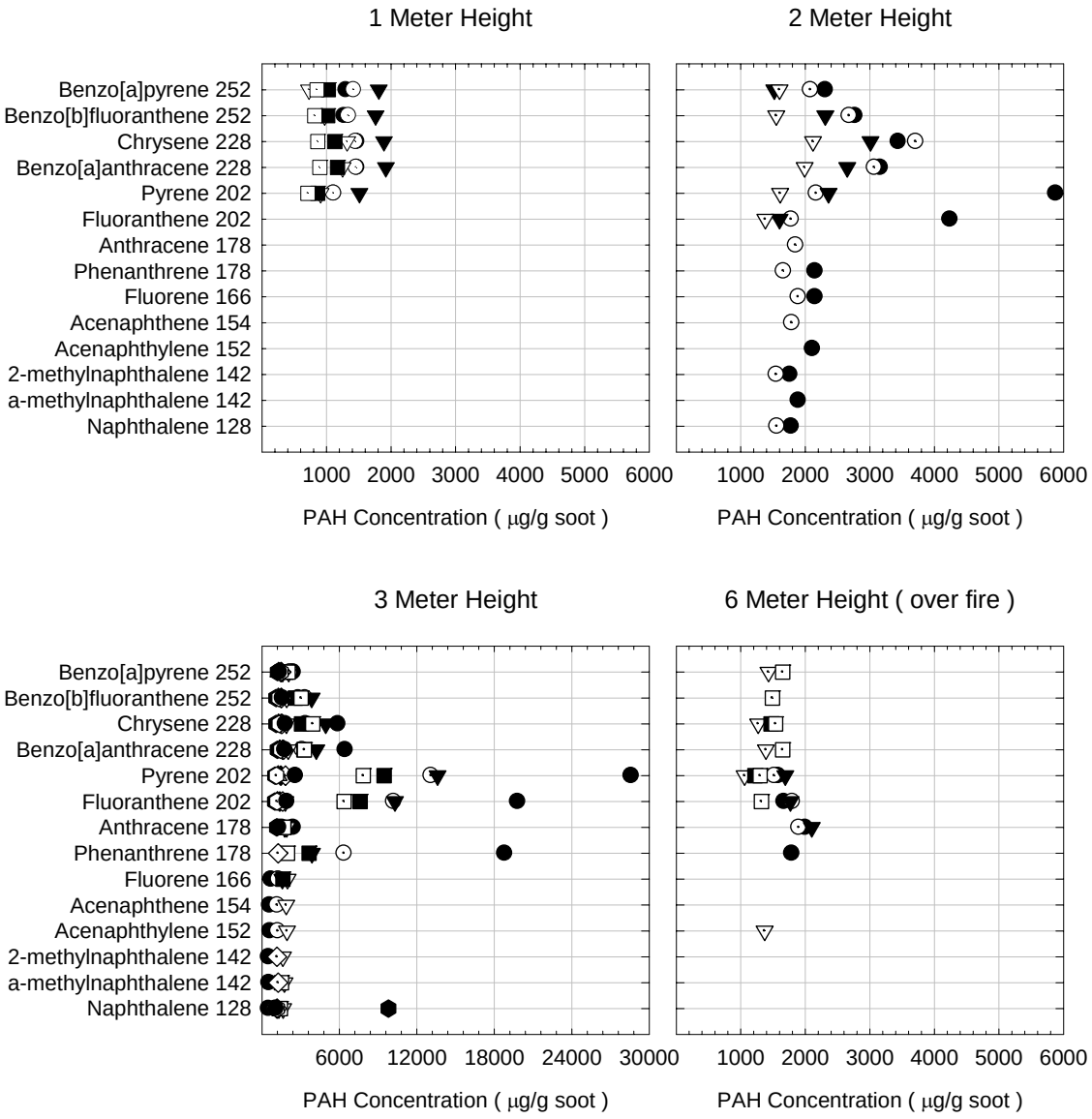

Figure 29. PAH concentrations in soot from multiple soot samples at each height.

Figure 30 depicts the average total concentration of the 14 PAHs at each height above the fuel pan. The vertical bars represent the standard deviations. The locations with the highest concentrations of PAH compounds are 2 m and 3 m above the fuel surface, and the amounts of PAH observed at these locations are similar. The 1 m and overfire locations also have similar concentrations of PAHs, but overall the concentrations are less than the concentrations at the other two locations. The trends in PAHs are remarkably similar to those of C/H ratio. In both the C/H and the PAH measurements, the 1 m and overfire regions were similar and the 2 m and 3 m locations were similar. The 2 m and 3 m locations have relatively high PAH concentrations, which is chemically consistent with a low C/H ratio. The relatively low PAH concentrations at the 1 m and overfire locations are consistent with a high C/H ratio. It is possible that the PAH material soluble in methanol/toluene is precursor-like material either adsorbed or chemically attached to the surface of the agglomerated soot at heights of 2 m and 3 m. The relatively large size of the primary particles at the 2 m location is consistent with a surface coating or commingled component of PAH material (i.e., precursor particle material). Concentrations of the five targeted stabilomers account for about half of the total measured PAH concentrations at every height shown in Figure 30.

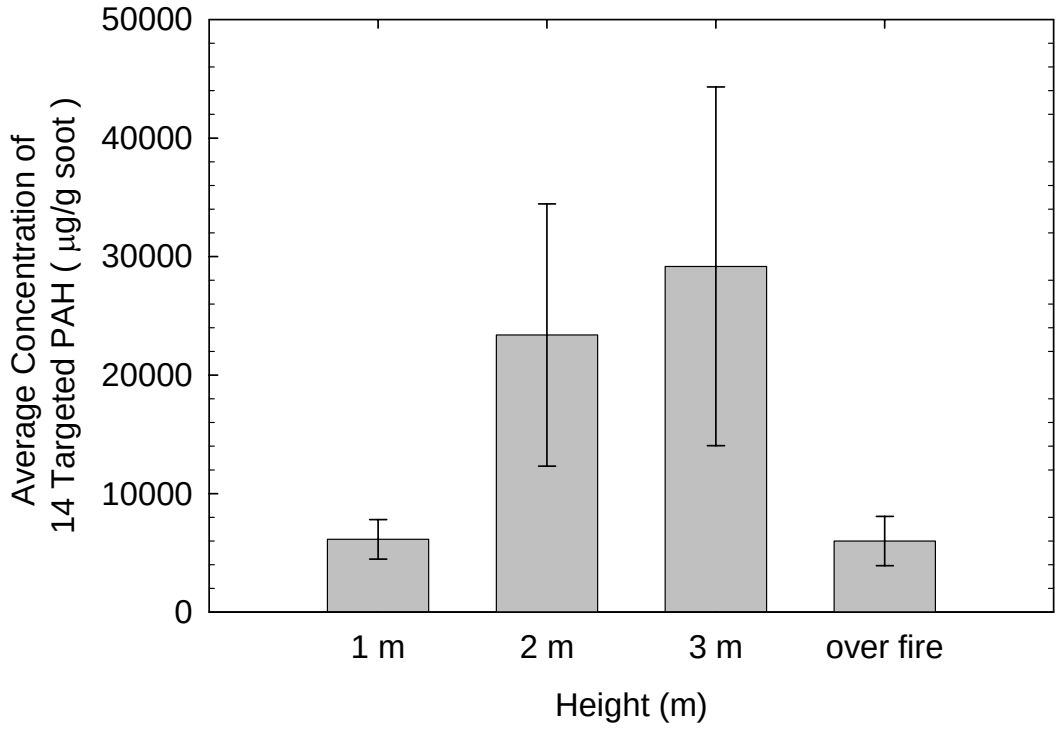

Figure 30. Average concentration of 14 targeted PAH in soot from a 2 m JP8 fire.

Average PAH isomer concentrations obtained at each height are summarized in Table 7. If the PAH concentration was below the detectable limit, a concentration of zero was used in the averaging. A graphical representation of the information in Table 7 is displayed in Figure 31. The compounds present in the greatest quantities have molecular weights of 178 g/mol, 202 g/mol and 228 g/mol. These three molecular weight groups contain major contributions from anthracene, pyrene, and chrysene—three of the targeted PAH that are also stabilomers (Stein and Fahr, 1985). (Accurate measurements of the fourth and fifth targeted stabilomers, naphthalene and acenaphthylene, are not possible presently because they are lighter molecules that may stay mostly in the gas phase at the filter temperature). The predominance of these compounds is consistent with their high thermodynamic stability at flame temperatures. The present results are consistent with the understanding that stabilomer PAHs persist at flame temperatures. The JP-8 pool fire PAH data are generally consistent with those of other flames.

With the exception of fluoranthene, no prominent peaks of the targeted PAH containing five-membered rings (acenaphthylene 152, acenaphthene 154, fluorine 166, and benzo-[b]fluoranthene 252) were observable in the present results. Similarly, no prominent peaks of the odd-carbon PAHs (1-methylnaphthalene 142, 2-methylnaphthalene 142, and fluorene 166) were observed. This result may mean that these compounds are not stable and are constantly appearing and disappearing within the fire (in contrast to the stabilomers that persist once they appear). It may also mean they have transformed into soot primary particles and no longer retain their identity, while the stabilomers, loosely attached to the soot, retain their identity when dissolved in methanol/toluene. The unanalyzed fraction of methanol/toluene-soluble material may consist of two- and three-membered rings linked into open structures as proposed by D'Anna et al. (2001), although this fraction was not recorded in the present work.

Table 7. PAH concentration summary in (μg/g soot).

Compound	MW	Formula	1 m	2 m	3 m	OF	Structure
Naphthalene*	128	$C_{10}H_8$	0	668	1700	0	
1-Methylnaphthalene	142	$C_{11}H_{10}$	0	378	420	0	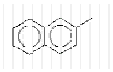
2-Methylnaphthalene	142	$C_{11}H_{10}$	0	662	274	0	
Acenaphthylene*	152	$C_{12}H_8$	0	422	315	228	
Acenaphthene	154	$C_{12}H_{10}$	0	358	304	0	
Fluorene	166	$C_{13}H_{10}$	0	808	596	0	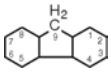
Anthracene*	178	$C_{14}H_{10}$	0	1400	2990	298	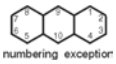
Phenanthrene	178	$C_{14}H_{10}$	0	916	1120	1000	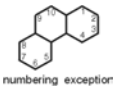
Fluoranthene	202	$C_{16}H_{10}$	0	3320	5360	1090	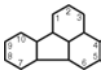
Pyrene*	202	$C_{16}H_{10}$	1030	2630	6970	1400	
Benzo[a]anthracene	228	$C_{18}H_{12}$	1360	3280	2620	507	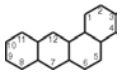
Chrysene*	228	$C_{18}H_{12}$	1350	3610	2640	713	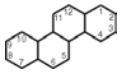
Benzo[a]pyrene	252	$C_{20}H_{12}$	1200	2770	2150	248	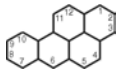
Benzo[b]fluoranthene	252	$C_{20}H_{12}$	1190	2150	1700	513	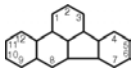

*Most stable isomer at flame temperatures (Stein and Fahr, 1985)

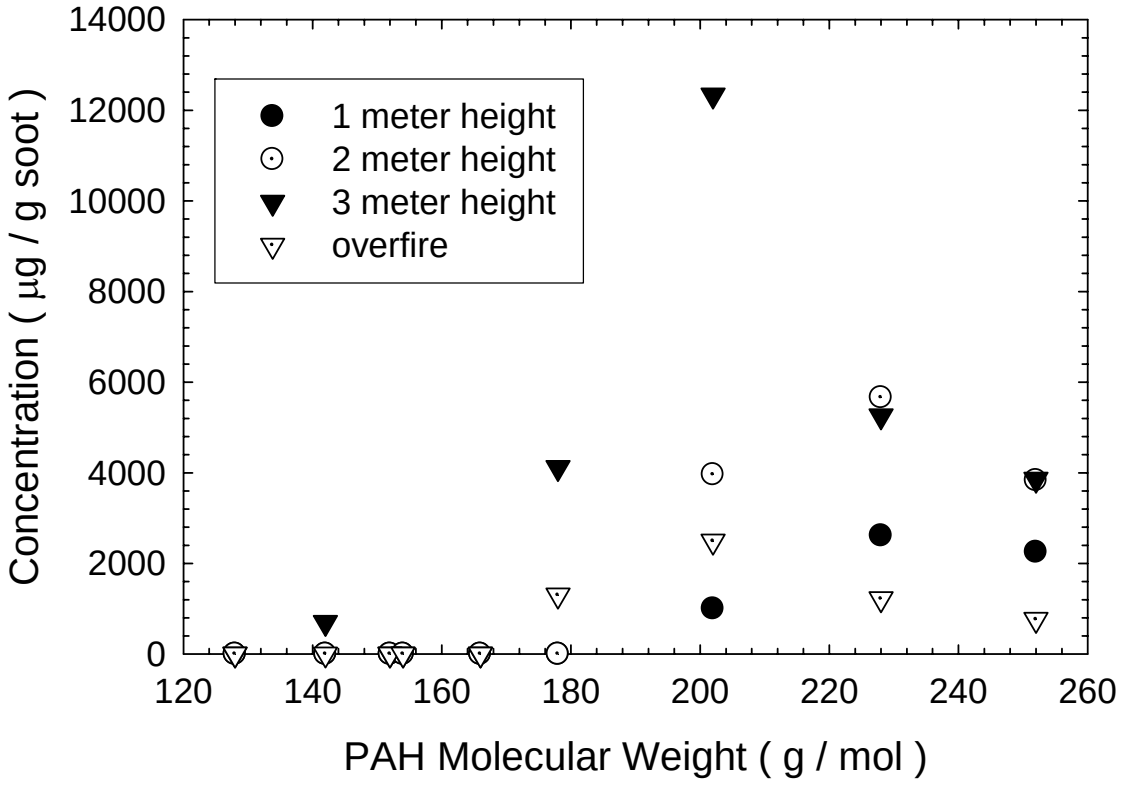

Figure 31. PAH concentrations in soot from a 2 m JP8 fire.

Soot Density

The density of soot within the fire was measured to determine if an appropriate value of density was being used in the extinction coefficient data reduction. The range of soot density values reported in the literature is 1.7-2.2 g/cm^3. The value used to calculate K_e in the experiments used was 1.74 g/cm^3. Data obtained as part of the density analysis was used to determine the uncertainty in the K_e measurement attributed to the assumed density value. Density analyses were performed by two individual laboratories. One sample was analyzed for the 1 m location and three samples were analyzed for the 2 m location. Difficulties with the collection procedure prohibited analysis of soot density at 3 m and overfire heights. At the 3 m location, soot was not deposited on the probe during the experiment so post-test collection procedures were not used. At the overfire location, the soot is sufficiently cool; therefore, it did not adhere to the probes.

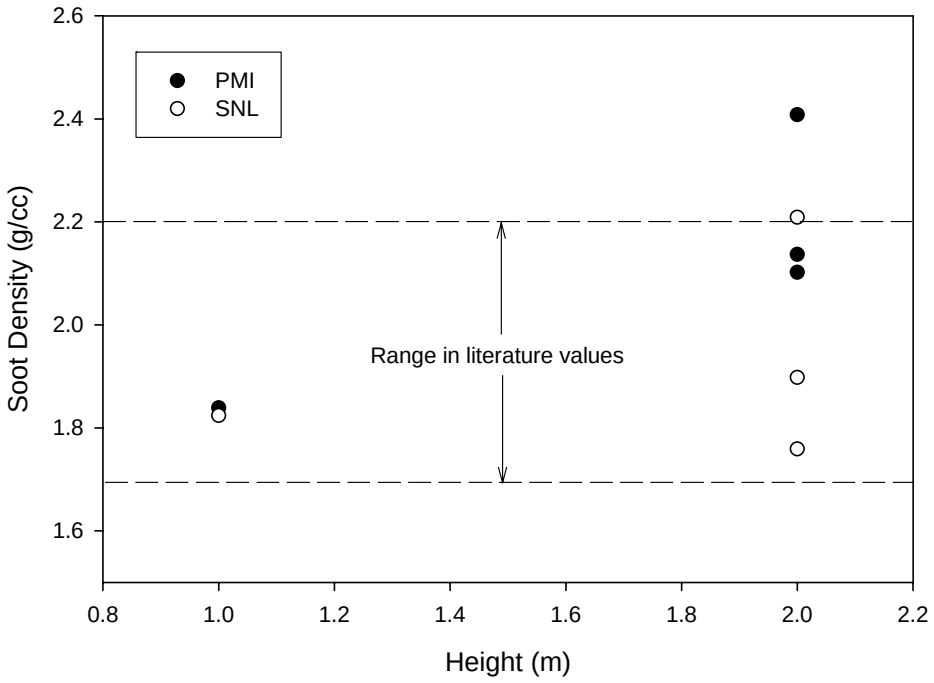

Figure 32. Soot density results.

Although there is considerable variability in the soot density results, shown in Figure 32, all of the measurements fall within the literature range except for one. The 1 m density results were remarkably consistent for the two laboratories. Each laboratory analyzed only one sample but the results were both 1.83±0.01 g/cm^3. There is considerable scatter in the 2 m results. This could be due to differences in the soot caused by turbulence or differences in the collection or analysis procedures. The average value and standard deviation for the 2 m location was 2.09±0.23 g/cm^3. The impact of density variations on the extinction coefficient calculations was assessed in the uncertainty section. The density results presented here are limited since it is difficult to collect a sufficient amount of soot for the analysis.

Predicted Scaling of Optical Properties with C/H Ratio

Modest (1993) presented a version of Rayleigh theory that includes a dispersion coefficient inversely proportional to C/H ratio. Modest showed that the extinction coefficient should be inversely proportional to the wavelength (expressed in μm) raised to the exponent of the dispersion coefficient. Using the equations from Modest, the relative scaling of the extinction coefficient can be predicted from the measured C/H ratios. Figure 33 depicts the results of such an analysis. Measured extinction coefficients in the figure are normalized by their measured values at the overfire height. Likewise, calculated extinction coefficients are expressed relative to their value at the overfire. The Modest scaling reveals that the extinction coefficient decreases with C/H ratio for wavelengths less than 1 μm and increases with increasing C/H for wavelengths greater than 1 μm. In agreement with this scaling rule, the trend in extinction coefficient qualitatively matches the trend in C/H ratio for a laser beam wavelength greater than 1 μm (1310 nm or 1.31 μm). For a wavelength less than 1 μm, the relative trends are reversed. The scaled extinction coefficients shown in the figure qualitatively track the measured trends. Hence, variations in soot optical properties with height can be partially attributed to the effect of soot chemistry changes on dispersion.

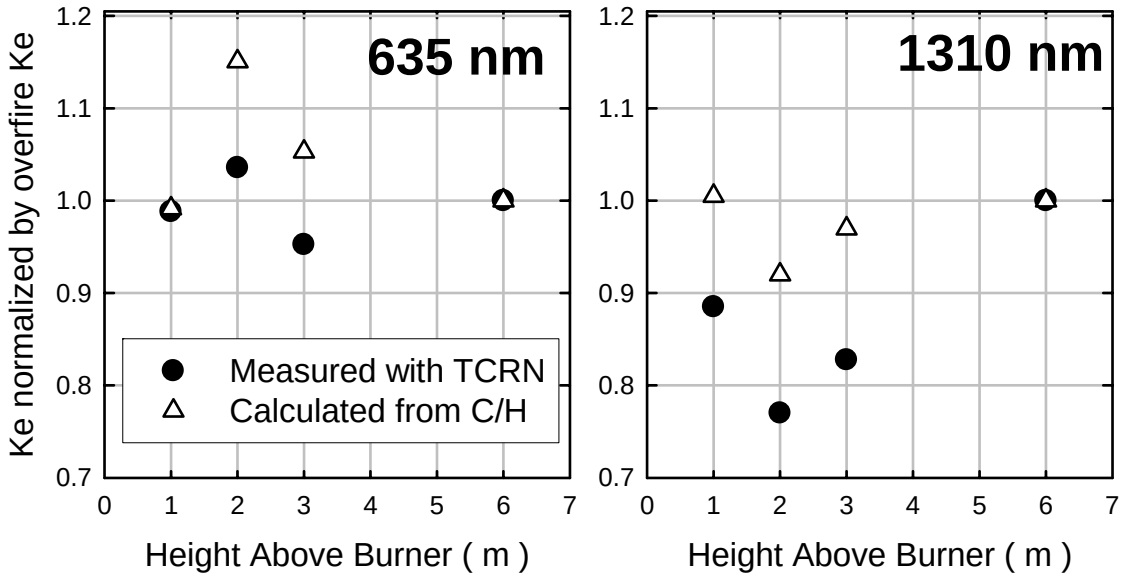

Figure 33. Measured and calculated relative extinction coefficients.

IX. Conclusions

This report detailed the measurement of the optical properties, morphology, and chemistry of soot collected from within 2 m diameter JP-8 pool fires at heights of 1 m, 2 m, 3 m ~6m (overfire) above the fuel surface. The dimensionless extinction coefficient, K_e, of soot at visible (635 nm) and near-infrared (1310 nm) wavelengths was measured using a transmission cell (TCRN). The TCRN was calibrated using polystyrene microspheres, and measured K_e values were within 8.8% of those predicted by Mie theory. The total Type B uncertainty in the TCRN-determined extinction coefficient was calculated to be 11.9%. It was demonstrated that soot morphology is not significantly affected by transport through the sampling system. The TCRN laser traces demonstrated good repeatability between fires. Ten extinction coefficient experiments were performed at each height in the flame zone and eleven at the overfire position in a JP-8 pool fire. In the overfire region, measured values for K_e of 8.4±1.2 at 635 nm and 8.7±1.1 agree well with the published values for post-flame JP-8 soot in laminar and turbulent flames. Measured K_e values at 635 nm showed little variation with location in the fire with an average of 8.35. Average K_e values in the infrared showed more variation with location, which is at least partially attributable to larger Type B uncertainties.

Samples were collected thermophoretically on TEM grids and subsequently analyzed to determine morphology and fractal dimensions. The primary particle diameter and aggregate radius of gyration varied with position in the fire. The particle sizes were greatest at the 2 m height and smallest at the 3 m height. The radius of gyration showed similar trends with location. Fractal prefactor and fractal dimension showed little variation with position in the fire. The prefactors measured varied from k_f =1.68 to 1.72, and the fractal dimension ranged from D_f =6.20 to 6.31. Both of these are consistent with overfire results in the literature. High-resolution TEM imaging was performed on soot collected at all locations, and qualitative changes in the nanostructure were apparent. The aggregates became more “filled in” with increasing height. Mixed aggregates with at least two primary particle sizes were observed at all heights in the fire. In general, aggregate morphology and primary particle sizes at the 2 m height were the most similar of those at all the heights to traditionally published overfire aggregates.

Measured K_e values were compared to predictions of the Rayleigh-Debye-Gans theory of scattering and absorption performed using the measured particle dimensions and literature values of soot optical properties (in the visible). The predicted trends in K_e with height in the fire are similar to those measured; however, in all cases, K_e was underpredicted by as much as 30%. Such discrepancy emphasizes the need for more accurate measurement of the refractive indices of soot, particularly in the near-IR, and the importance of direct measurement of optical properties using a sampling technique.

The C/H ratio of sampled soot increased as height increased from 2 m to 6 m. Measured C/H ratios were between 4:1 and 8:1, which are greater than those of precursor particles and similar to those measured for young soot aggregates (Dobbins et al., 1998). This

finding is consistent with the fact that aggregates were found at every height using TEM analysis. The PAH concentrations exhibited trends similar to those of the C/H ratios: Where C/H was high (1 m and overfire), PAH concentrations were low. Where C/H was low (2 m and 3 m), PAH concentrations were high. Of the PAH targeted, the five stabilomers made up about 50% of the mass of the 14 PAH. The most abundant PAHs of the 14 targeted ones had molecular weights of 178 g/mol, 202 g/mol, and 228 g/mol. These contain major contributions from targeted stabilomers. No prominent trends were observed in the five targeted PAH that contained five-membered rings or in the three targeted PAH with odd numbers of carbon atoms. The findings confirm the importance of PAH stabilomers at flame temperatures and suggest that soot carbonizes as it traverses the fire vertically. A change in optical properties may accompany the carbonization. Rayleigh theory combined with a C/H-ratio-dependent dispersion coefficient qualitatively predicts the measured trends in extinction coefficient. Measured densities of physically sampled soot were 1.83 $\pm$ 0.01 g/cm^3 at 1 m and 2.09 $\pm$ 0.23 g/cm^3 at 2 m above the fuel pan. Although there was considerable variability in the soot density results, all of the measurements fall within the literature range (1.7-2.2 g/cm^3) except for one. The uncertainty in the K_e measurement is impacted by the uncertainty in the value of the soot density; therefore, a more detailed study of soot density would be beneficial.

This study represents the first set of measurements of the dimensionless extinction coefficient and morphology of soot in both the flame zone and overfire regions of large, fully-turbulent fires. The relatively constant value of K_e near 8.0 to 8.5 at both 635 nm and 1310 nm provide confidence in the use of a single dimensionless extinction coefficient in the SIERRA/Fuego models of radiative transport from high temperature soot emission. The soot morphology sampled in the large fires is similar to the literature for the overfire region of smaller turbulent flames for which it has been shown that scattering contributes approximately 20% to the total extinction, and, therefore, neglecting it in the Fuego model appears reasonable.

X. References

Blanchat, T.K., Characterization of the Air Source and Plume Source at FLAME, SAND2001-2227. Sandia National Laboratories, Albuquerque, NM, July 2001.

Blevins, L.G., Fletcher, R.A., Benner, B.A., Steel, E.B., and Mulholland, G.W. "*The Existence of Young Soot in the Exhaust of Inverse Diffusion Flames*" Proceedings of the Combustion Institute, Vol. 29, pp. 2325-2333, 2002.

Bohren, C.F. and Huffman, D.R., Absorption and Scattering of Light by Small Particles, 1983.

Calcote, H.F., "Mechanisms of Soot Nucleation in Flames—A Critical Review," Combustion and Flame, Vol. 42, pp. 215-242, 1981.

Choi, personal communication regarding per-pixel analysis (2002 and 2003).

Choi, M.Y., Mulholland, G.W., Hamins, A. and Kashiwagi, T., "*Comparisons of the Soot Volume Fraction Using Gravimetric and Light Extinction Techniques*," Combustion and Flame, Vol. 102, pp. 161-169, 1995.

Ciajolo, A., D'Anna, A., and Barbella, R., "*PAH and High Molecular Weight Species Formed in a Premixed Methane Flame*," Combustion Science and Technology, Vol. 100, pp. 271-281, 1994.

Coleman and Steele. Experimentation and Uncertainty Analysis for Engineers, 1999.

D'Anna, A., Violi, A., D'Alessio, A., and Sarofim, A.F., "*A Reaction Pathway for Nanoparticle Formation in Rich Premixed Flames*," Combustion and Flame, Vol. 127, pp. 1995-2003, 2001.

Dobbins, R.A., Fletcher, R.A., and Chang, H.C., "*The Evolution of Soot Precursor Particles in a Diffusion Flame*," Combustion and Flame, Vol 115, pp. 285-298, 1998.

Dobbins, R.A. and Megaridis, C.M., "*Morphology of Flame-Generated Soot as Determined by Thermophoretic Sampling*," Langmuir 3, 254-259, 1987.

Dobbins, R.A. and Megaridis, C.M. "*Absorption and Scattering of Light by Polydisperse Aggregates*," Applied Optics, Vol 30, No. 33, 1991.

Dobbins, R.A., Mulholland, G.W., and Bryner, N.P. "*Comparison of a Fractal Smoke Optics Model with Light Extinction Measurements*," Atmospheric Environment, Vol. 28, pp. 889-897, 1994.

Faeth, G.M., and Köylü, Ü.Ö., "*Soot Morphology and Optical Properties in Nonpremixed Turbulent Flame Environments*," Combusiton Science and Technology, Vol. 108, pp. 207-209, 1995.

Frenklach, M., "*Reaction Mechanism of Soot Formation in Flames*," Physical Chemistry Chemical Physics, Vol. 4, No. 11, pp. 2028-2037, 2002.

Glassman, I., "*Soot Formation in Combustion Processes*," Twenty-Second Symposium (International) on Combustion, The Combustion Institute, 1988, pp. 295-311;

Haynes, B.S., and Wagner, H.G., "*Soot Formation*," Progress in Energy and Combustion Science, V. 7, pp. 229-273, 1981.

Hochrein, J. and Borek, T. Student Symposium Presentation, Sandia National Laboratories, August 2003.

Kennedy, I.M., "*Models of Soot Formation and Oxidation*," Progress in Energy and Combustion Science, V. 23, pp. 95-132, 1997.

Köylü, U.O., and Faeth, G.M. "*Radiative Properties of Flame Generated Soot*", Journal of Heat Transfer, Vol. 115, pp. 409-417, 1993.

Köylü, U.O., Faeth, G.M., Farias, T.L., and Carvalho, M.G. "*Fractal and Projected Structure Properties of Soot Aggregates*," Combustion and Flame, Vol. 100, pp. 621-633, 1995.

Krishnan, S.S., Lin, K.-C., and Faeth, G.M., "*Optical Properties in the Visible of Overfire Soot in Large Buoyant Turbulent Diffusion Flames*," Journal of Heat Transfer, Vol. 122, pp. 517-524, 2000.

Lee, S.H., Nam, J.J., and Son, B.M., "*Feasibility of the Simultaneous Determination of Polycyclic Aromatic Hydrocarbons by Near Infrared Spectroscopy*," Bulletin of the Korean Chemical Society, Vol. 24, pp. 246-248, 2003.

Manzello, S. L., and Choi, M.Y., "*Morphology of Soot Collected in Microgravity Droplet Flames*," Internation Journal of Heat and Mass Transfer, Vol. 45, No. 5, pp. 1109-1116, 2002.

Modest, M.F., Radiative Heat Transfer. McGraw-Hill, New York, 1993.

Mulholland, G.W., and Bryner, N. P., "*Radiometric Model of the Transmission Cell-Reciprocal Nephelometer*," Atmospheric Environment, Vol. 28, No. 5, pp. 873-887, 1994.

Mulholland, G.W., and Choi, M.Y., "*Measurement of the Mass Specific Extinction Coefficient for Acetylene and Ethene Smoke Using the Large Agglomerate Optics Facility*," Proceedings of the 27th Symposium (International) on Combustion, The Combustion Institute, August 2-7, Boulder, CO, 1515-1522, 1998.

Richter, H. and Howard, J.B. "*Formation of Polycyclic Aromatic Hydrocarbons and their Growth to Soot – A Review of Chemical Reaction Pathways*," Progress in Energy and Combustion Science, Vol. 26, pp. 565-608, 2000.

Sander, L.C., and Wise, S.A., Polycyclic Aromatic Hydrocarbon Structure Index, NIST Special Publication 922, National Institute of Standards and Technology, Gaithersburg, Maryland, 1997.

Smyth, K.C. and Shaddix, C.R., "*The Elusive History of m=1.57-0.56i for the Refractive Index of Soot*," Brief Communication, Combustion and Flame, Vol. 107, pp. 314-320, 1996.

Stein, S.E., and Fahr, A., "*High Temperature Stabilities of Hydrocarbons*," Journal of Physical Chemistry, Vol. 89, pp. 3714-3725, 1985.

Taylor, B.N. and Kuyatt, C.E. "*Guidelines for Evaluating and Expressing the Uncertainty of NIST Measurement Results*," NIST Technical Note 1297, 1994.

Tieszen, S.R., Black, A.R., Moen, C.D., Chu, T.Y., Nicolette, V.F., Gill, W., Burns, S.P., Moffatt, W.C., and Gritzo, L.A., "*SIERRA/FUEGO and SIERRA/SYRINX Verification and Validation Plan Version 2.0*", SAND2001-3798, December, 2001, (OFFICIAL USE ONLY).

Vander Wal, R.L. and Tomasek, A.J., "*Soot Nanostructure and its Impact Upon the O_2 Oxidation Rate*," Proceedings of the Seventh International Workshop on Microgravity Combustion and Chemically Reacting Systems, NASA Report NASA/CP-2003-212376, pp. 41-44, 2003.

Williams, J.M. and Gritzo, L.A. "*In-Situ Sampling and Transmission Electron Microscope Analysis of Soot in the Flame Zone of Large Pool Fires*," 27th International Symposium on Combustion, 1998.

Zhu, J., Choi, M.Y., Mulholland, G.W., and Gritzo, L.A. "*Measurement of Soot Optical Properties in the Near-Infrared Spectrum*," International Journal of Heat and Mass Transfer, 43, pp. 3299-3303, 2000.

Distribution

1	MS0886	Ted Borek	1822
1	MS0886	James Hochrein	1835
1	MS1135	Louis Gritzo	9132
5	MS1135	Kirk Jensen	9132
1	MS1135	Dann Jernigan	9132
5	MS1135	Jill Suo-Anttila	9132
1	MS1135	Sheldon Tieszen	9132
1	MS1146	Tom Blanchat	9132
1	MS9052	Chris Shaddix	8367
5	MS9052	Linda G. Blevins	8367
1	MS9053	Peter Witze	8362
1	MS9055	Hope Michelsen	8351
1	MS9055	Donald Hardesty	8360
1	MS0384	Tom Bickel	9100
1	MS0824	Jaime Moya	9130
1	MS0828	Martin Pilch	9133
1	MS9052	Jay Keller	8367

1 Mun Young Choi
Professor and Head of Mechanical Engineering and Mechanics
Drexel University
3141 W. Chestnut Street, 115 Curtis Hall
Philadelphia, PA 19104

1 George Mulholland
National Institute of Standards and Technology
100 Bureau Drive, Stop 8662
Gaithersburg, MD 20899-8662

1 Randall VanderWal
National Aeronautics and Space Administration
Glenn Research Center
21000 Brookpark Rd
Cleveland, OH 44135

1 John DeRis
FM Global Research
1511 Boston-Providence Hwy.
Norwood, MA 02062

1 Richard Dobbins
Brown University
Box D
Providence, RI 02912

1 Adel Sarofim
University of Utah
Combustion Research Group
Kennecott Building
1515 Mineral Sq Rm 207
Salt Lake City, UT 84112

1	MS9018	Central Technical File	8945-1
2	MS0899	Technical Library	9616